

## ABSTRACT

Dissertation:

### STUDIES OF THE OPTICAL PROPERTIES OF PLASMONIC NANOSTRUCTURES

Yu-Ju Hung, Doctor of Philosophy, 2007

Directed By:

Professor Christopher C. Davis  
Department of Electrical and Computer  
Engineering

Various properties of Surface Plasmon Polaritons (SPPs) at the interface between a layer of PMMA (polymethyl methacrylate) gratings and a 50 nm thick gold film have been studied. Gold has a negative dielectric constant at visible wavelength range which results in negative refraction phenomenon without medium of both permittivity ( $\epsilon$ ) and permeability ( $\mu$ ) constants negative. A direct observation of negative refraction has been demonstrated. It verifies our assumption that in the 1-D stripe PMMA gratings on top of a gold film, SPPs experience negative group velocity and positive phase velocity. With this criterion, negative refraction is the natural choice in Snell's Law. Correspondingly, it was previously claimed that with a highly anisotropic layered structure (metal/dielectric stack), the high spatial frequency  $k$  vectors scattered from an object can be preserved in an imaging system and the conventional diffraction limit is defeated. In this dissertation, this kind of layered

structure, a so-called “hyperlens” or “superlens”, has been experimentally demonstrated and the results verify theoretical predictions. A proof of concept on corner resonators has also been demonstrated. Four squares with PMMA/Au and Air/Au are arranged so that SPPs are trapped in the corner. It shows the possibility of making a tiny resonator with zero phase paths in the cavity.

An experiment utilizing the field enhancement of SPPs is designed. A surface field is excited on R6G(Rhodamine 6G, fluorophore)/PMMA gratings/Au substrate. The enhanced pumping light pushes up the emission intensity 10-fold or higher compared to a sample with a R6G/PMMA gratings/Glass platform, a transparent substrate. This device with a R6G/PMMA gratings/Au platform has the advantage that the emission light is converted to the normal direction; the collection efficiency is high and the directivity makes the examination easy under a commercial fluorescence optical microscope. This device shows the potential of R6G/PMMA/Au platforms in gene chip industry.

STUDIES OF THE OPTICAL PROPERTIES OF  
PLASMONIC NANOSTRUCTURES

By

Yu-Ju Hung

Dissertation submitted to the Faculty of the Graduate School of the  
University of Maryland, College Park, in partial fulfillment  
of the requirements for the degree of  
Doctor of Philosophy  
2007

Advisory Committee:  
Professor Christopher C. Davis, Chair  
Professor Mario Dagenais  
Professor Ping-Tong Ho  
Dr. Balzano Quirino  
Professor Robert W. Gammon

© Copyright by  
Yu-Ju Hung  
2007

## Dedication

To my family.

## Acknowledgements

I would like to thank my advisor, Chris, for his guidance and encouragement of my research work. The years at Maryland have been quite wonderful. Chris gives students a nice learning environment and his open-minded attitude toward students really nourished my Ph.D. life. Secondly, I would like to thank Dr. Smolyaninov for his intuitive suggestions on my research work. Without Igor's keen reminding, I would have spent much time dwelling on some situations which new people easily get stuck on. Igor's focusing on the frontier research gave me a great position in my research work. Also, I would like to thank Dr. Quirino Balzano, the experienced vice president from the Motorola Research Lab. With Dr. Q's enthusiasm and sharp thinking, I learned how to focus on the key points quickly and think about the real physical meaning of my Surface Plasmon Polariton work. During cold Decembers, I will miss Dr. Q's parties, which were very memorable. Dr. Vildana's and Dr. Gammon's timely help at the fluorescence work are greatly appreciated. Dr. Vildana's warm encouragement on research always lit my inner candle and I wish that I can be a blessing toward other people, especially women in the science field. I would like to thank my previous advisor, Dr. Ping-Tong Ho. Without Dr. Ho's support in the first two years at Maryland, I would never come to UMD.

Over the years, MOG group members, Shawn, Sugi, Heba, Jamie, John, Felice, Ehren and Yohan provided numerous encouragements, jokes, and favors. I would like to offer my thanks specifically to the Nano-Carbon Tube group at the Physics Department. Dr. Furer's generosity made the E-beam lithography work easy and

convenient. The graduate students, Yung-Fu, Tarek and Chuan helped me with the AFM work a lot. Other friendly members, Adrian, Dan, Goken, Dave, Todd and Sung-Jae gave a lot of suggestions. I would like to thank my previous lab members: Vien and Rohit who taught me the clean room processing skills. Also, I would like to thank my friends, Li-Chiou, Li-Chuan, Roger, Hsin-Hua, Hsung-Chen and Hsin-Yun for numerous encouragements in life which always lifted me up. I am so lucky that I met all of them at Maryland. Finally, I would like to thank my family members: Dad, sis, and my brothers. Many international calls made me regain the bravery to proceed on my Ph.D. path. I thank God who brought me to Maryland and has me in His plan.

Publication List:

- [1] Igor I. Smolyaninov, Yu-Ju Hung, and Christopher C. Davis, “**Magnifying superlens in the visible frequency range**”, *Science*, Vol.315, 23 March 2007.
- [2] Igor I. Smolyaninov and Yu-Ju Hung, “**Enhanced transmission of light through a gold film due to excitation of standing surface-plasmon Bloch waves**”, *Physical Review B* 75, 033411, 2007.
- [3] Yu-Ju Hung, Igor I. Smolyaninov, Hsuan-Chen Wu, and Christopher C. Davis, “**Fluorescence enhancement by surface gratings**”, *Optics Express*, Vol.14, No.22, pp.10825, 2006.
- [4] Igor I. Smolyaninov, Yu-Ju Hung, and Christopher C. Davis, “**Super-resolution optics using short-wavelength surface Plasmon polaritons**”, *Journal of Modern Optics*, Vol. 53, No.16-17, 10-20, pp. 2337, 2006.
- [5] Igor I. Smolyaninov, Yu-Ju Hung, and Christopher C. Davis, “**Light-induced resonant transmittance through a gold film**”, *Applied Physics Letters*, 87,041101,2005.
- [6] Igor I. Smolyaninov, Yu-Ju Hung, and Christopher C. Davis, “**Surface plasmon dielectric waveguides**”, *Applied Physics Letters*,87,241106,2005.

Conference Papers

- [7] Yu-Ju Hung, Igor I. Smolyaninov, and Christopher C. Davis, “**Focusing of Surface Plasmon Polaritons by Surface Parabolic Dielectric Gratings**”, *CWC5, Plasmonics and Metamaterials, CLEO, Baltimore, 2007.*
- [8] Igor I. Smolyaninov, Yu-Ju Hung, and Christopher C. Davis, “**Fluorescence enhancement by surface gratings**”, *QThE5, Plasmonics II, CLEO, Baltimore, 2007.*
- [9] Igor I. Smolyaninov, Yu-Ju Hung, and Christopher C. Davis, “**Magnifying Superlens in the Visible Frequency Range**”, *JMA4, Plasmonic Nanophotonics, CLEO, Baltimore, 2007.*
- [10] Igor I. Smolyaninov, Yu-Ju Hung, and Christopher C. Davis, “**Magnifying Superlens in the Visible Frequency Range**”, *OSA Topical Meeting: Photonic Metamaterials, Wyoming, 2007.*
- [11] Igor I. Smolyaninov, Yu-Ju Hung, and Christopher C. Davis, “**Dielectric optical devices for plasmon polariton optics**”, *(Invited Talk) SPIE, Aug. 2006.*
- [12] Yu-Ju Hung, Igor I. Smolyaninov, Hsuan-Chen Wu, and Christopher C. Davis, “**Fluorescence enhancement by surface gratings**”, *SPIE, Aug. 2006.*
- [13] Igor I. Smolyaninov, Yu-Ju Hung, and Christopher C. Davis, “**Surface plasmon dielectric waveguides**”, *Session P 36: Plasmon Resonances in Nanostructures, APS March Meetings, 2006.*
- [14] Yu-Ju Hung, Igor I. Smolyaninov, and Christopher C. Davis, “**Strong optical coupling effects through a continuous metal film with a surface dielectric grating**”, *Proc.SPIE Vol. 5927, pp. 386-394, Plasmonics: Metallic Nanostructures and Their Optical Properties III, Aug. 2005.*
- [15] Quirino Balzano, Yu-Ju Hung, Igor I. Smolyaninov, , and Christopher C. Davis, “**Fourier analysis of plasmon polariton propagation in periodic structures of nanoholes**”, *JTuC108, CLEO 2005.*



## Table of Contents

Dedication .....	ii
Acknowledgements .....	iii
Table of Contents .....	vi
List of Tables .....	vii
List of Figures .....	viii
Chapter 1: Introduction .....	1
Surface Plasmon Polaritons .....	1
Motivation and Summary of Work .....	3
Chapter 2: Basic Transmission Properties - Strong Optical Coupling Effects through Continuous Metal Film with a Surface Dielectric Grating .....	5
Introduction .....	5
Dispersion Relation .....	5
Sample Preparation and Optical Setup .....	13
Results and Discussion .....	14
Application I: Light Concentrator and Coupling Device .....	19
Application II: Nonlinear Signal Processing of Enhanced Transmission .....	25
Chapter 3: Two-Dimensional Negative Refractive Index Device in the Optical Frequency Range .....	26
Introduction to Left-Handed Materials .....	26
<i>Characteristics of the Negative Refractive Effect</i> .....	27
<i>Dispersion Relation of Dielectric/Gold/Dielectric Structure</i> .....	34
Experimental Evidence of a Negative Refractive Index .....	37
<i>Snell's Law with Negative Refraction</i> .....	37
<i>Focusing Effect on Concentric Rings</i> .....	39
<i>Magnifying Superlens in the Visible Frequency Range</i> .....	43
<i>Interference Effect on Two Focusing Devices</i> .....	49
<i>Corner Resonators</i> .....	52
Conclusion .....	54
Chapter 4: Fluorescence Enhancement using Surface Gratings .....	55
Introduction .....	55
Experiment .....	58
<i>Comparison between a Grating Deposited onto a Metal Layer and an         Evanescent Grating Coupler</i> .....	58
<i>Polarization and Periodicity Dependence</i> .....	61
<i>Rotation of Incident Angle</i> .....	65
Discussion .....	70
Chapter 5: Conclusion .....	74
Bibliography .....	77

## List of Tables

2.1 The incident and collection angles for various spectral peak wavelengths .....	25
2.2 The theoretical $k_{sp}$ for each peak wavelength.....	28
4.1 The relation between the coupling order $n$ and the image intensity.....	83

## List of Figures

2.1 structure of plasmonic device.....	16
2.2 two-layered structure.....	18
2.3 Dispersion of the SPP field .....	19
2.4 Sample structure.....	19
2.5 Field distribution on a thin metal film.....	20
2.6 Dispersion relation for symmetrical and anti-symmetrical field.....	22
2.7 AFM picture of the PMMA gratings.....	24
2.8 Optical setup of the spectrum measurement.....	24
2.9 Efficient coupling output at the surface grating area.....	25
2.10 Spectrum - Incident angle = $8.5^\circ$ .....	26
2.11 Spectrum - Incident angle = $31^\circ$ .....	26
2.12 Dispersion relation of symmetrical field and the experimental data fitting.....	28
2.13 Geometric optics of a reflective-type parabolic lens.....	30
2.14 Parabolic PMMA mirror.....	31
2.15 Dielectric waveguide formed with the parabolic PMMA mirror.....	32
2.16 Structure used in simulation.....	33
2.17 Propagation length of SPP modes.....	34
2.18 Light-induced resonant transmission on an $\text{As}_2\text{S}_3$ glass.....	35
3.1 Dispersion relation of SPP on gold/Glass semi-infinite interface.....	37
3.2 Negative and Positive refractive index material.....	39
3.3 Wave front alternation in negative refractive index material.....	37
3.3 Field distribution of SPP modes on a thin metal film.....	41
3.4 Dispersion relation of Symmetrical mode on two three-layered structures.....	43
3.5 Dispersion relation of Symmetrical mode on two three-layered structures.....	44
3.6 Images of the devices .....	45
3.7 Incident angle $40^\circ$ for $\lambda = 488\text{nm}$ .....	46
3.8 AFM image of the concentric rings.....	48
3.9 AFM image of the rings.....	49
3.10 488 nm unbalanced case.....	50
3.11 The simulation structure with different incident angles.....	50
3.12 Optical paths for different $n_1/n_2$ ratio.....	50
3.13 phase matching condition on the half-ring device .....	52
3.14 Hyperlens effect on the half-circular gratings.....	53
3.15 Control experiment with no SPP source in the center.....	54
3.16 Resolution analysis on the superlens effect.....	56
3.17 Con-focal parabolic gratings with inner focal length $10\ \mu\text{m}$ .....	57
3.18 A serial experiment on parabolic gratings.....	58
3.19 The checkerboard structure.....	60
3.20 The light confinement at the corner resonator structure .....	61
3.21 The checkerboard structure.....	61
3.22 Light confinement in the corner resonator structure.....	64
4.1 Evanescent wave coupling structure.....	65
4.2 Fluorescence efficiency at precise and arbitrary angle coupling.....	66
4.3 Surface-Plasmon Coupled Emission.....	67
4.4 Coupling angle for each laser wavelength.....	67

4.5 Surface-Plasmon Coupled Emission setup and the emission angle.....	68
4.6 Device structures on ITO and Gold substrate. ....	69
4.7 Illustration of devices and optical setup.....	69
4.8 The intensity of R6G/PMMA gratings on ITO and Au/glass substrate.....	71
4.9 Polarization setup.....	72
4.10 Fluorescence under normal excitation .....	73
4.11 Polarization effect on gratings with normal incidence to the sample surface.....	73
4.12 Polarization effect on the sample.....	74
4.13 The geometry of the incident laser beam and angle definitions.....	76
4.14 Rotation effect on fluorescence enhancement.....	76
4.15 Fluorescence emission vs. angle $\alpha$ .....	80
4.16 Illustration of momentum matching condition.....	82
4.17 $k^*$ for different order $n$ .....	82

# Chapter 1: Introduction

## *Surface Plasmon Polaritons*

With the prevalence of nano-tools, such as e-beam lithography, focused ion beam (FIB), atomic-force microscopes (AFM), near-field scanning optical microscopes (NSOM) and tunneling-electronic microscopes (TEM), science research has entered a tiny world on a nanometer scale. How small is this? Comparing 10 nm to 1 m is the same as comparing 10 cm to the earth's diameter. In the past, optical behavior has been studied down to the micrometer scale, which is in the visible light range. We know that scattering and diffraction happen when the object size is on the same order of the impinging light wavelength. However, when the dimension of an object is in the nanometer range, a lot of optical properties change. For example, from Ebbesen's reports<sup>1,2</sup> in Nature 1998 and 2003, showed that there was enormous transmission (1000 times higher than predicted by existing theory) through an optically thick Au film if there are sub-wavelength periodic holes in it. Actually even a single hole has excess transmission. These kinds of effects were contradictory to our understanding of transmission through sub-wavelength holes based on theory developed by Bethe<sup>3</sup> in 1944. Another interesting example is that color saturation in dye solutions can be enhanced if metal nano-particles are added in due to surface Plasmon resonances. These findings tell us that we need to fill gaps in our understanding of optical behavior on scales ranging from Angstrom-size atoms to micron-scale objects. Visible light cannot penetrate well through metals, but the metal/air interface can support electromagnetic waves that possess peculiar properties. Surface waves generated on metal nano-particles or on nano-structures are of considerable current

interest and much research is focused on these phenomena. More over, due to the short effective wavelength of surface Plasmon polaritons, (or surface plasmons as they are often called), nano-optical circuits integrated with electronics appear to be possible. Recently, there have been many studies of “negative refraction” phenomena on surface plasmons involving consideration of loss mechanisms, which have opened the door to an entire field of sub-wavelength imaging.

What is a Surface Plasmon Polariton (SPP)? Let's start with a more familiar object- a plasma. A plasma is a neutral ionized gas. Electrons are free in the ionized medium. A plasmon is the quasi-particle resulting from the quantization of plasma oscillations. Plasmons are collective waves of the free electron gas density, which often occur at optical frequencies. A collective wave is the opposite of a single quasi-particle interaction. It is usually used to describe a plasma. As waves or as an organized motion of the plasma, particles within the plasma can interact at long ranges through electric and magnetic forces. A Polariton is an excitation involving one quantized mode strongly coupled with another: for example, Phonon-Polaritons result from coupling visible light with an exciton; and a Surface Plasmon-Polariton, results from coupling of surface plasmons with light. A Surface Plasmon Polariton is a classical solution of Maxwell's equations- a charge density wave (a surface electro-magnetic wave) excited at an interface between a metal or doped semiconductor with an appropriate (real part negative) complex dielectric constant, and a medium with a positive dielectric constant above the negative layer .

## *Motivation and Summary of Work*

In this dissertation, the properties of SPP waves on two-dimensional structures have been studied. Fluorescence enhancement due to SPP wave excitation has been observed and characterized. A 10-fold, or higher, intensity enhancement had been achieved when the exciting light is coupled into a SPP mode. This shows the possibility of efficiency improvements in bio-molecule detection. With a regular fluorescence optical microscope, the enhancement can be seen without a complicated optical setup, which makes the technique easy to implement when compared to other techniques<sup>4-9</sup>. In this dissertation, a different regime of SPP behavior has been studied. Previously most calculations have been about long range surface plasmons, in which only the real part of the metal dielectric constant is considered (the imaginary part is neglected). And, it is been assumed that for gold, in the region between 480 nm to 530 nm, SPPs are very lossy and are not very useful because of losses. However, in this thesis, when loss is included, negative refractive index behavior has been found on planar meta-structures. This originates from the abnormal dispersion curve in a specific wavelength region. In 2000, John Pendry<sup>11</sup> proposed that negative refractive materials can enhance the evanescent waves and that the resolution of the image in a negative refractive index “lens” can be improved by the resultant increase of collected spatial frequencies. These early proposals for a “superlens” did not consider the unavoidable losses in real materials. The design and fabrication of negative refractive materials is extremely complicated. Before 2007, it had only been implemented in the radio-frequency range. Attempts have been made to try to improve the design by using so-called “double negative” material (both negative  $\epsilon$  and  $\mu$ ) in the optical frequency range, but the losses are still high. In 2006, an

alternative design using a highly anisotropic layered medium was proposed and theoretically showed the ability to resolve objects beyond the diffraction limit. In this thesis, negative refractive behavior has been observed at a wavelength of 532 nm. Later on, a 2-D circular layered lens with positive and negative refractive indices was fabricated and showed its ability to resolve small objects with a 130 nm spacing. This lens is called a “hyperlens” or “superlens”<sup>10~12</sup>, which overcomes the diffraction limit (the resolution is  $\sim \lambda/8$  in the experiments reported in this dissertation). To our knowledge, this is the first experimental demonstration of a two-dimensional “superlens” or “hyperlens” that acts as an imaging device. In addition, I have designed various 2-D plasmonic structures, which offer an easy way to demonstrate negative refractive index devices without a complicated design.

In Chapter 2, the fundamental eigenmodes of SPPs at a two layer (Au/air) interface and for three layers (dielectric1/Au/dielectric2) are derived and the dispersion curves are shown. PMMA(dielectric) nano-gratings are patterned on a PMMA/Au film. The enhanced transmission effect due to SPP/free space wave coupling is measured. SPPs are coupled into a small waveguide by using a 2-D parabolic light concentrator. Chapter 3 discusses negative refraction phenomena and many interesting planar devices are shown. Chapter 4 deals with fluorescence enhancement due to SPP excitation. Since a SPP is a localized surface wave, the surface field is strong and fluorescence enhancement should be observed if a thin layer of fluorophore material is used. Fluorescence enhancement on different grating pitches was demonstrated and shows the possibility of intensity enhancement for bio-molecule detectors. Future work and a summary of my research are included in chapter 5.



## **Chapter 2: Basic Transmission Properties - Strong Optical Coupling Effects through a Continuous Metal Film with a Surface Dielectric Grating**

### *Introduction*

Enhanced light transmission through subwavelength holes in metal films once was a somewhat controversial issue. Different theoretical descriptions of this phenomenon have invoked such effects as SPP excitation and various diffraction effects<sup>1,2,9</sup>. The main feature of the transmission spectrum through a metal film with an array of nanoholes is suppression and enhancement ( $10^3$  times) of optical transmission at a set of wavelengths, which span a spectrum range. In the SPP picture of the enhanced transmission, the reciprocal lattice vector of the nanohole array provides the phase matching condition for SPP generation. Thus, the transmission of nanohole arrays is highly selective. The opposite claim is that no SPP is involved in this extraordinary transmission effect, only diffraction effects, i.e. the coupling between evanescent waves and radiation fields<sup>9</sup>. However, a lot of experiments can be explained by adopting the SPP model<sup>1</sup>. Relatively few papers adopt the pure evanescent wave coupling effect for their results.

### *Dispersion Relation*

In this chapter, the basic eigensolutions of two layered and three layered structures are derived here from the continuity conditions of Maxwell's equations. Measurements of the transmission spectrum and simulation of a three layered structure have been described<sup>4</sup> in this thesis. The structure is shown in Fig 2.1 with a 50 nm gold layer and a layer of PMMA gratings on top. Similar samples have been investigated before by several groups<sup>14 ~ 17</sup>. PMMA is polymethyl methacrylate, one kind of electron-beam resist, purchased

from Micro-Chem. The enhanced transmission with P-polarized excitation observed in these papers indicates that the SPP mechanism is involved<sup>14</sup>. The dispersion relation of the reflected wave, which has been recorded by direct imaging, shows that SPPs have been excited<sup>15</sup>. These measurements show a forbidden band gap in the transmission spectrum, which demonstrates the interaction between the photonic crystal structure and SPPs. In addition, an optimum thickness for the maximum transmission has been observed<sup>16</sup>, which favors the SPP-based mechanism. A basic transmission spectrum measurement of the device shown in Fig. 2.1 has been performed here at two different incident angles. This device structure is used for several experiments described in this thesis; therefore it is worth studying its transmission properties at the beginning.

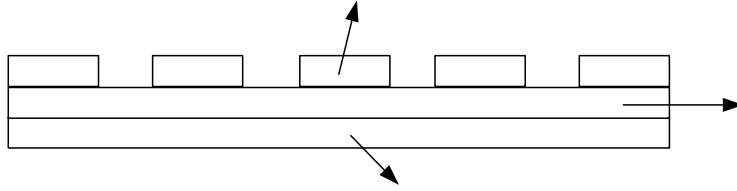


Figure 2.1: structure of a plasmonic device.

First, we deal with a two layered structure as shown in Fig 2.2. The interface lies on the x-y plane with upper medium  $\varepsilon_1$  and lower medium  $\varepsilon_2$ . The wave propagates in the x direction only and the E field in the x, z plane. We can write the field as:

$$\begin{aligned}
 E_1 &= (E_{x1}, 0, E_{z1}) \exp[i(k_x x - \omega t)] \exp(ik_{z1} z) \\
 H_1 &= (0, H_{y1}, 0) \exp[i(k_x x - \omega t)] \exp(ik_{z1} z) \\
 E_2 &= (E_{x2}, 0, E_{z2}) \exp[i(k_x x - \omega t)] \exp(ik_{z2} z) \\
 H_2 &= (0, H_{y2}, 0) \exp[i(k_x x - \omega t)] \exp(ik_{z2} z),
 \end{aligned} \tag{1}$$

where  $k^2 = k_x^2 + k_z^2$ .

Applying Maxwell's equation  $\nabla \cdot E = 0$ , we get:

$$E_{z1} = -E_{x1} k_x / k_{z1}, \quad E_{z2} = -E_{x2} k_x / k_{z2}. \quad (2)$$

$$\text{with } \nabla \times E = -\mu \frac{\partial H}{\partial t} \quad \text{with } \mu \cong \mu_0, \quad (3)$$

we find:

$$H_{y1} = \omega E_{x1} \varepsilon_1 \varepsilon_0 / k_{z1}, \quad H_{y2} = \omega E_{x2} \varepsilon_2 \varepsilon_0 / k_{z2}. \quad (4)$$

The tangential  $H$  and tangential  $E$  are continuous, thus  $H_{y1} = H_{y2}$  and  $E_{x1} = E_{x2}$ , leading

to the simple equations:

$$\varepsilon_1 / k_{z1} = \varepsilon_2 / k_{z2}$$

$$\text{with } k_{z1} = -i(k_x^2 - \varepsilon_1 k^2)^{1/2},$$

$$\text{and requiring } k_x^2 > \varepsilon_1 k^2 ;$$

$$k_{z2} = -i(k_x^2 - \varepsilon_2 k^2)^{1/2},$$

$$\text{requiring } k_x^2 > \varepsilon_2 k^2$$

In the above equations:

$$k_x = k \sqrt{\varepsilon_1 \varepsilon_2 / (\varepsilon_1 + \varepsilon_2)}$$

$$\text{with } \varepsilon_2 < 0 \text{ and } |\varepsilon_2| > \varepsilon_1.$$

Equation (7) is the basic dispersion relation of a two layered structure.

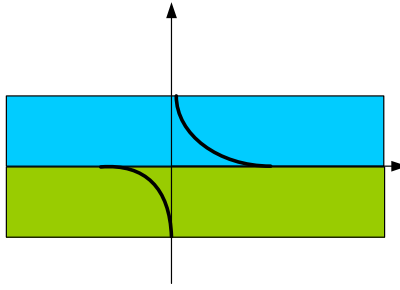


Figure 2.2: two-layered structure.

Fig. 2.3 shows the dispersion curve for a two layered structure. The asymptotic form drawn as a dash line shows up when only the real part of the metal dielectric constant is considered. In this figure, the layers are gold and a dielectric material with a refractive index 1.5. By plugging in the complex form of the gold dielectric constant, the dispersion curve starts to approach the light line but with a backward wave region. The group velocity and phase velocity have opposite signs in the backward wave region, which shows negative refractive behavior. This property gives us a lot of interesting phenomena in 2-D plasmonic devices.

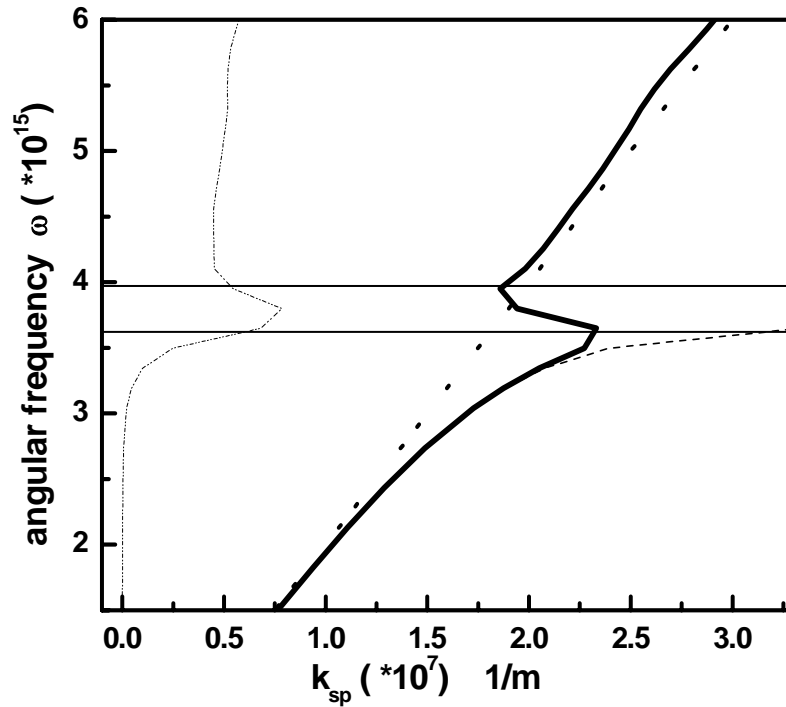


Figure 2.3: Dispersion of the SPP field on a semi-infinite Au film with dielectric material on top. The dot line (.....) is the light line, and the solid line (—) is the SPP mode with complex dielectric constant taken from<sup>19-1\*</sup>. The dash line (-----) is calculated with the real part of the Au dielectric constant taken from<sup>19-1</sup>. The dash-dot-dot line (— · — · —) is the imaginary k vector of SPP with complex dielectric constant.

For a three-layered structure<sup>18</sup>,

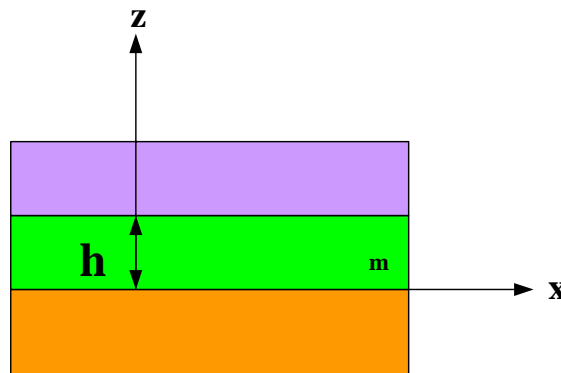


Figure 2.4: three-layered structure.

\* A more updated metal optical constants can be found in E.D. Palik's book<sup>19-2</sup>.

$$\bar{H} = \bar{y}f(z)\exp[i(\omega t - kx)] \quad (8)$$

$$E_x = \frac{i}{\omega\epsilon_0\epsilon} \frac{\partial H_y}{\partial z}, E_z = -\frac{k}{\omega\epsilon_0\epsilon} H_y \quad (9)$$

And the depth distribution is written as:

$$\begin{aligned} \epsilon_1 : f(z) &= e^{S_1 z}, z < 0 \\ \epsilon_m : f(z) &= \cosh(S_2 z) + \frac{S_1 \epsilon_m}{S_2 \epsilon_1} \sinh(S_2 z), 0 > z > h \\ \epsilon_3 : f(z) &= [\cosh(S_2 h) + \frac{S_1 \epsilon_m}{S_2 \epsilon_1} \sin(S_2 h)] e^{-S_3(z-h)}, z > h \end{aligned} \quad (10)$$

Where  $S_1, S_2$  and  $S_3$  are expressed as follows:

$$S_1^2 = k^2 - \epsilon_1 k_0^2, S_2^2 = k^2 - \epsilon_m k_0^2, S_3^2 = k^2 - \epsilon_3 k_0^2. \quad (11)$$

By continuity of  $E_x$  and  $H_y$ , we can get the dispersion relation  $\omega(k)$  out of the transcendental equation as follows:

$$\tanh(S_2 h) = [S_2 \epsilon_m (S_1 \epsilon_3 + S_3 \epsilon_1)] / (S_2^2 \epsilon_1 \epsilon_3 - S_1 S_3 \epsilon_m^2) \quad (12)$$

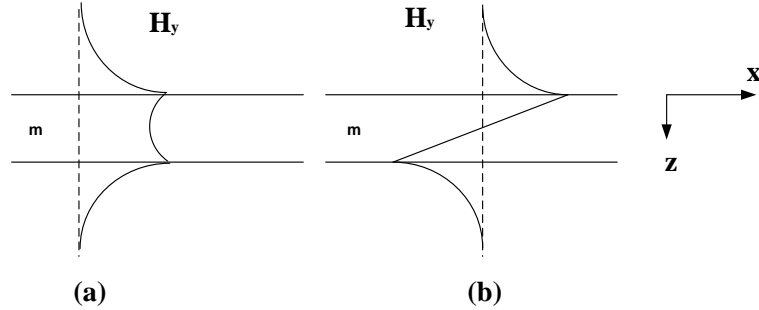
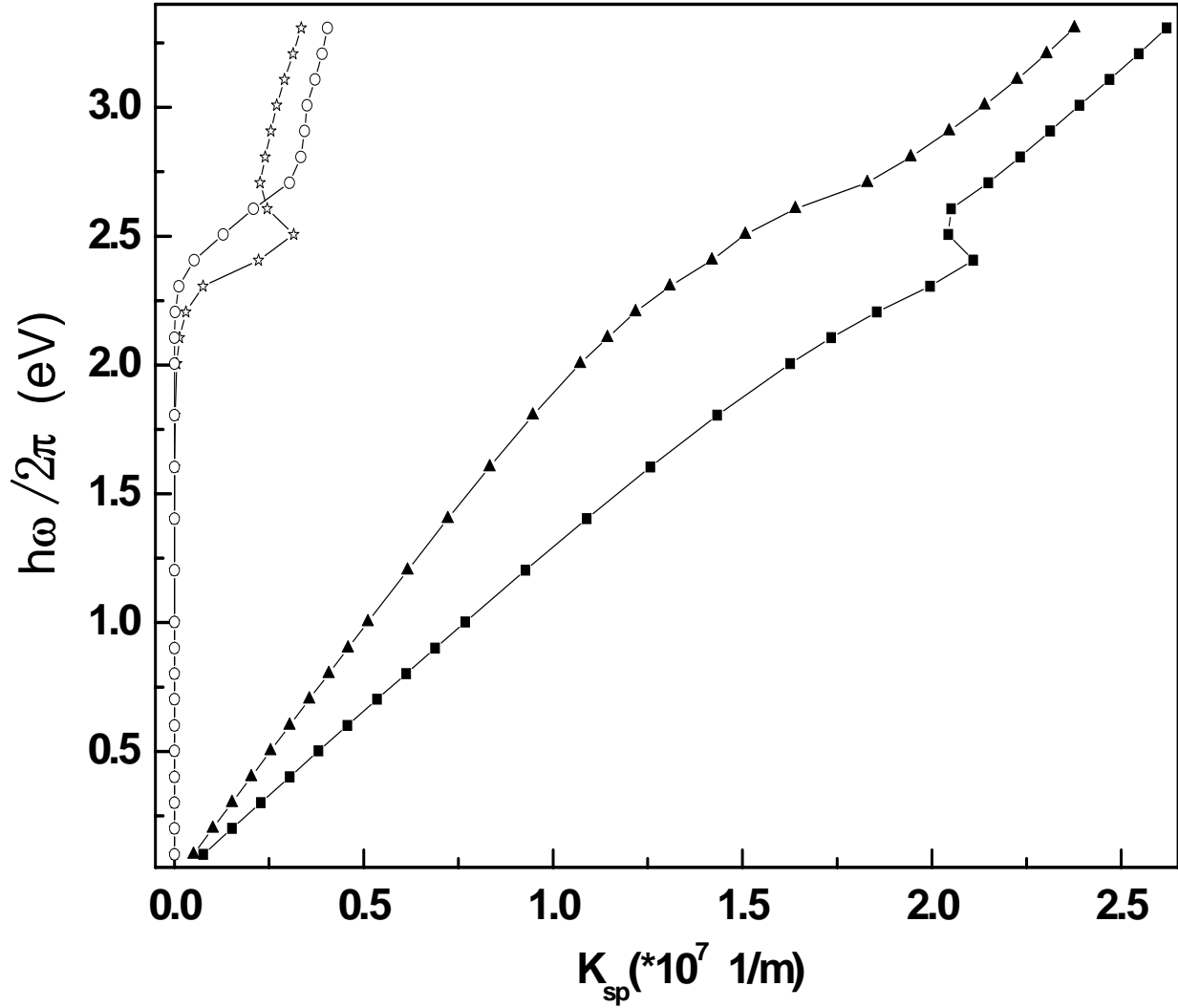


Figure 2.5: Field distribution of symmetric and anti-symmetric SPP modes on a thin metal film.

By plugging the real value of  $\epsilon_1, \epsilon_3$  and  $\epsilon_m$ , the first two roots with low absorption loss can be classified as symmetrical and anti-symmetrical fields shown in Fig 2.5. The dispersion

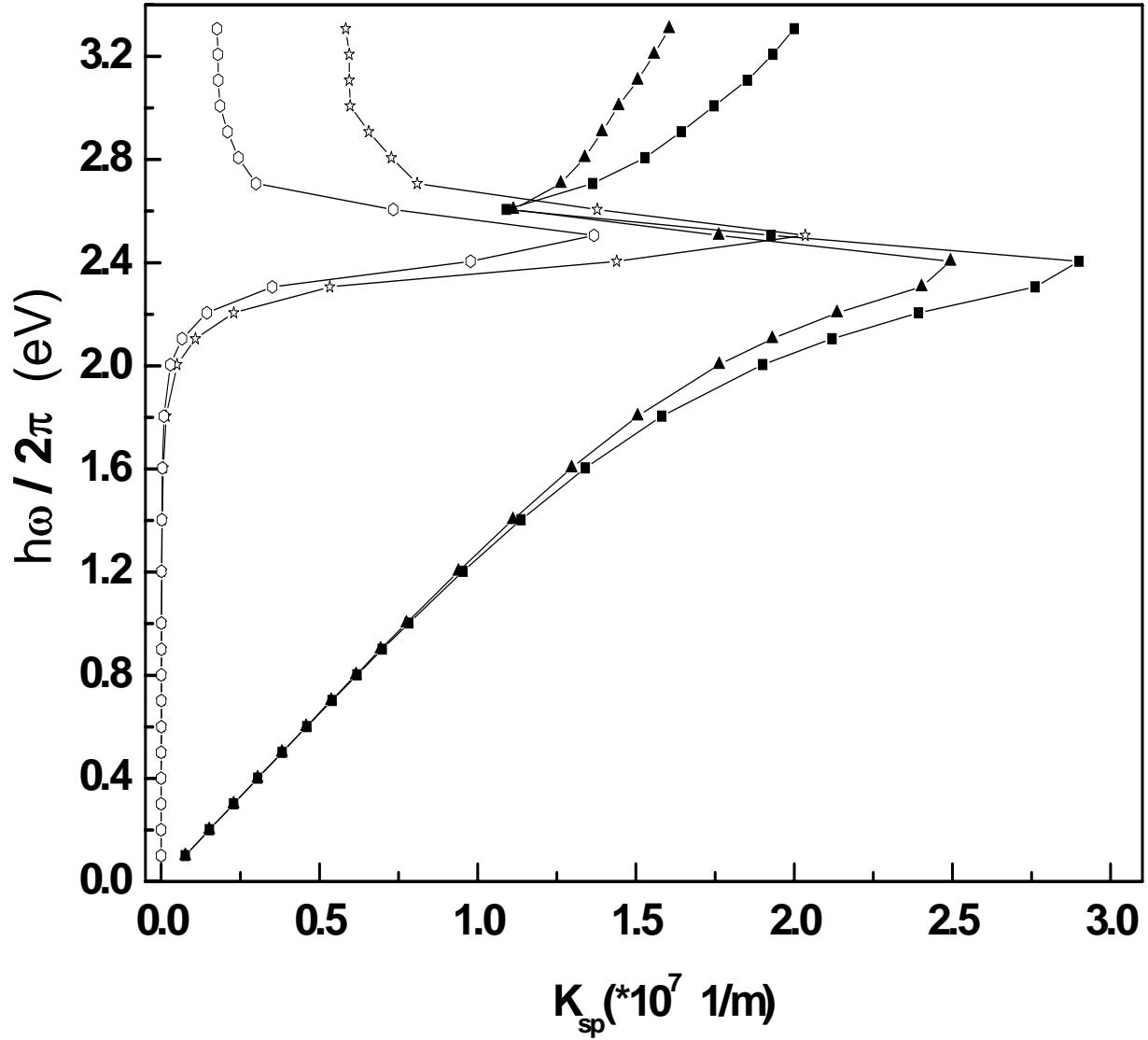
relations of the two modes can be plotted as in Fig 2.6. Here we plot Air (n=1)/Au/Glass (n=1.5) and PMMA (n=1.5)/Au/Glass (n=1.5).



(a)

Figure 2.6: Dispersion relation (a) symmetrical field

- Real part of  $k_{sp}$  with  $\epsilon_1 = 2.25$  and  $\epsilon_3 = 2.25$ .
- ☆— Imaginary part of  $k_{sp}$  with  $\epsilon_1 = 2.25$  and  $\epsilon_3 = 2.25$ .
- ▲— Real part of  $k_{sp}$  with  $\epsilon_1 = 2.25$  and  $\epsilon_3 = 1.0$ .
- Imaginary part of  $k_{sp}$  with  $\epsilon_1 = 2.25$  and  $\epsilon_3 = 1.0$ .



(b)

Figure 2.6: Dispersion relation (b) anti-symmetrical field.

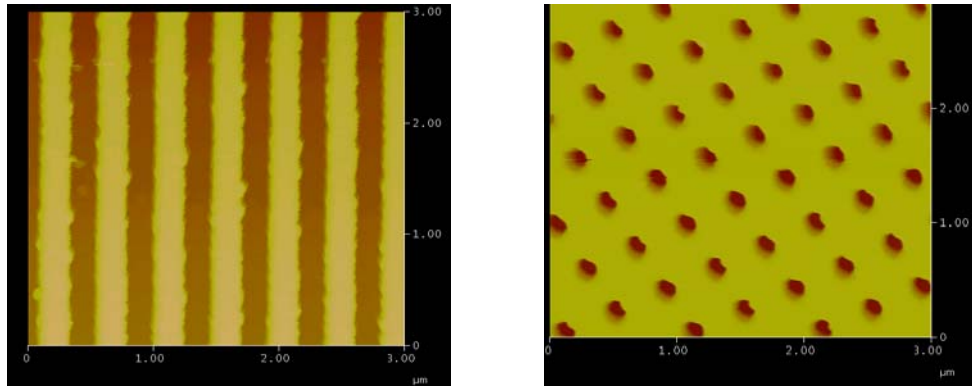
- Real part of  $k_{sp}$  with  $\varepsilon_1 = 2.25$  and  $\varepsilon_3 = 2.25$ .
- ☆— Imaginary part of  $k_{sp}$  with  $\varepsilon_1 = 2.25$  and  $\varepsilon_3 = 2.25$ .
- ▲— Real part of  $k_{sp}$  with  $\varepsilon_1 = 2.25$  and  $\varepsilon_3 = 1.0$ .
- Imaginary part of  $k_{sp}$  with  $\varepsilon_1 = 2.25$  and  $\varepsilon_3 = 1.0$ .



## *Sample Preparation and Optical Setup*

A 50 nm thick gold film was sputtered onto a glass substrate using an AJA Magnetron Sputtering Machine. An overlay PMMA film was then spin-coated and patterned by using a JEOL310 Electron Beam system located in Dr. Fuhrer's lab in the Physics Department. The e-beam resist used here is 495PMMA A4 (4% in Anisole) from Microchem. The AFM images of the patterned gratings are shown in Fig. 2.7. The dielectric film is about 200 nm thick. Film thickness is determined by the spinning system. The grating pitch is 500 nm. The gold film under the PMMA layer was still intact after the gratings were developed using MIBK/IPA (3:1) developer from Microchem.

Our optical setup is shown in Fig. 2.8. A halogen lamp is used as a white light source. A lens with 100 mm focal length is used to collimate the white light. The sample with a PMMA grating faces the incident light and the diffracted transmitted light is collected on the back side of the sample. The cleaved end of a multimode fiber (50/125  $\mu\text{m}$ -core/cladding) with an aperture is placed at the focal point of a collection lens with 50 mm focal length (see Fig. 2.8 (a)). The sample was located far enough from the illumination source and from the collection aperture, so that the incident and collection angles were well-defined ( $\pm 0.5$  degrees).



(a)

(b)

Figure 2.7: AFM picture of the PMMA gratings (a) stripe gratings. (b) bi-gratings.

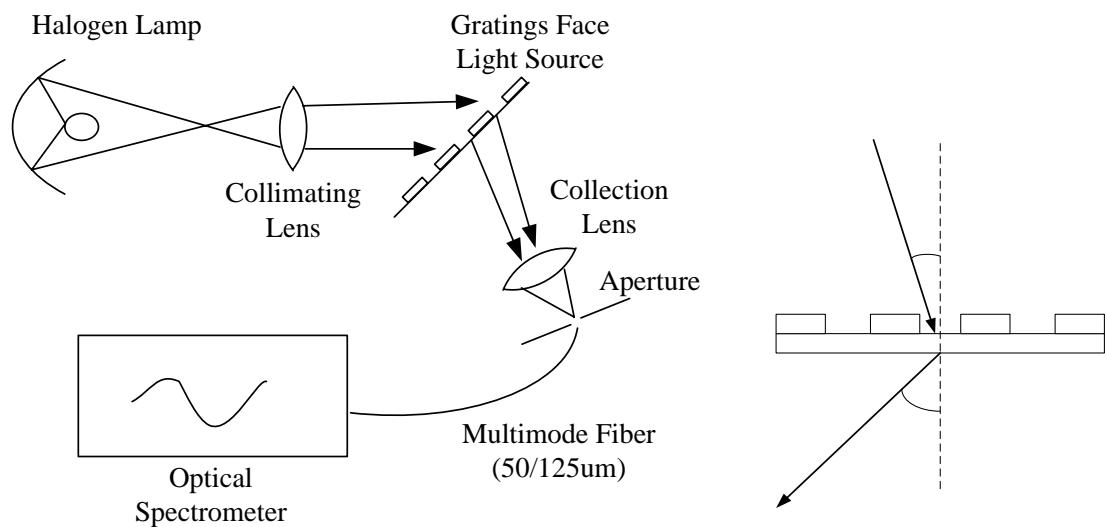


Figure 2.8: Optical setup for spectrum measurement.

### *Results and Discussion*

Enhanced transmission has been observed with incident light illumination from either the front or back side of the sample. A typical transmission pattern is shown in Fig 2.9.

488nm laser light illuminates the sample from the back side and only the grating area shows relatively large coupling output.

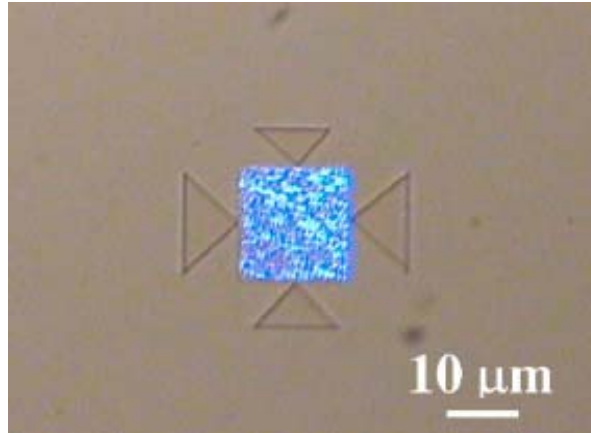


Figure 2.9: Large coupling output through the surface grating area.

However, the enhanced transmission was observed to be more pronounced with illumination of the front side of the sample (the side on which the dielectric grating lies). A higher SPP excitation rate occurs with front illumination of the sample<sup>1, 19</sup> because less light is reflected back from the corrugated surface and much light get transmitted through. The measured spectra at various incident angles are shown in Figs. 2.10 and 2.11. The incident and collection angles are listed in Table 2.1.

Incident Angle ( $^{\circ}$ ): 8.5		Incident Angle ( $^{\circ}$ ): 31	
$\lambda$ (nm)	Collection Angle( $^{\circ}$ )	$\lambda$ (nm)	Collection Angle( $^{\circ}$ )
515	67	610	54.2
490	52.2	575	52.5
420	42.5	530	42

Table 2.1: The incident and collection angles for various spectral peak wavelengths.

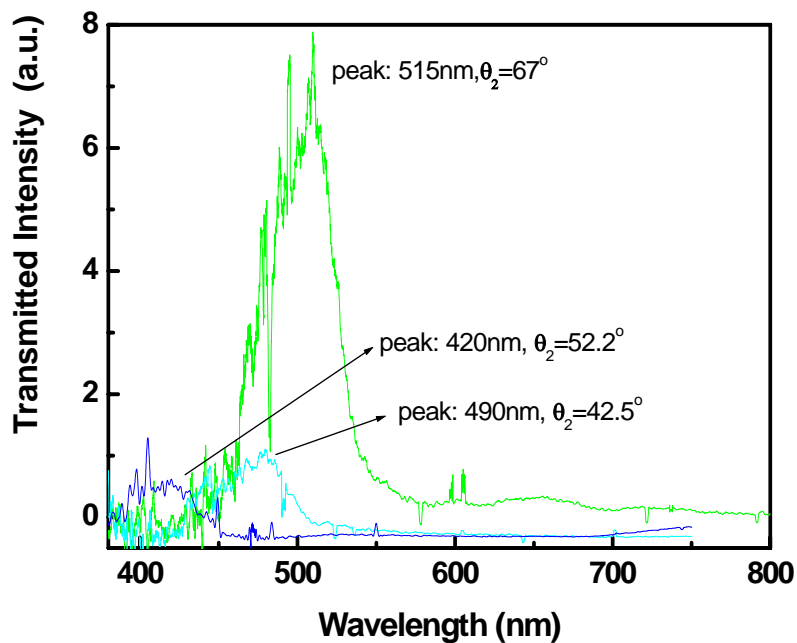


Figure 2.10: Spectrum - Incident angle =  $8.5^\circ$

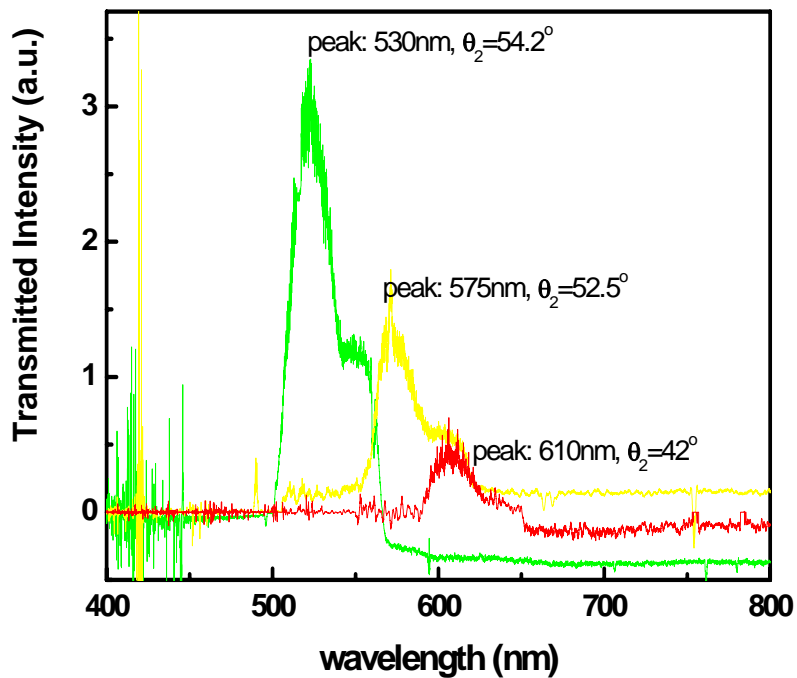


Figure 2.11: Spectrum - Incident angle =  $31^\circ$

The dispersion curves of the symmetrical and anti-symmetrical fields are solved based on the transcendental equations shown in Eq. (12). The imaginary part of the propagation constant of anti-symmetrical fields is very large so no data points are fitted as anti-symmetrical field excitations.

By examining the phase matching condition:

$$\pm k_{sp} = k_o \sin \theta \pm n\bar{G} \quad (13)$$

Where  $k_{sp}$  is the symmetrical SPP propagation constant,  $k_o = 2\pi/\lambda$ ,  $\bar{G} = 2\pi/a$ , and  $a = 500$  nm is the periodicity of the PMMA grating, we can characterize the generation of SPP modes at specific incident angles. Although in our experiments the transmission signals were spectrally continuous, we can still measure well-defined spectral peaks at certain collection angles. We believe that these peak values correspond to SPP generation, while both diffraction and SPP effects are actually involved in the overall process. The results are shown in Fig 2.12. The error bars of the experimental points are the full-width-half-maximum (FWHM) of each representative peak in the spectrum. Two kinds of structures are involved: PMMA/Au/Glass and Air/Au/Glass. Both real and imaginary parts of propagation constants are shown in the figure. The experimental measurements are shown as the hollow triangle with proper order  $n$  chosen.

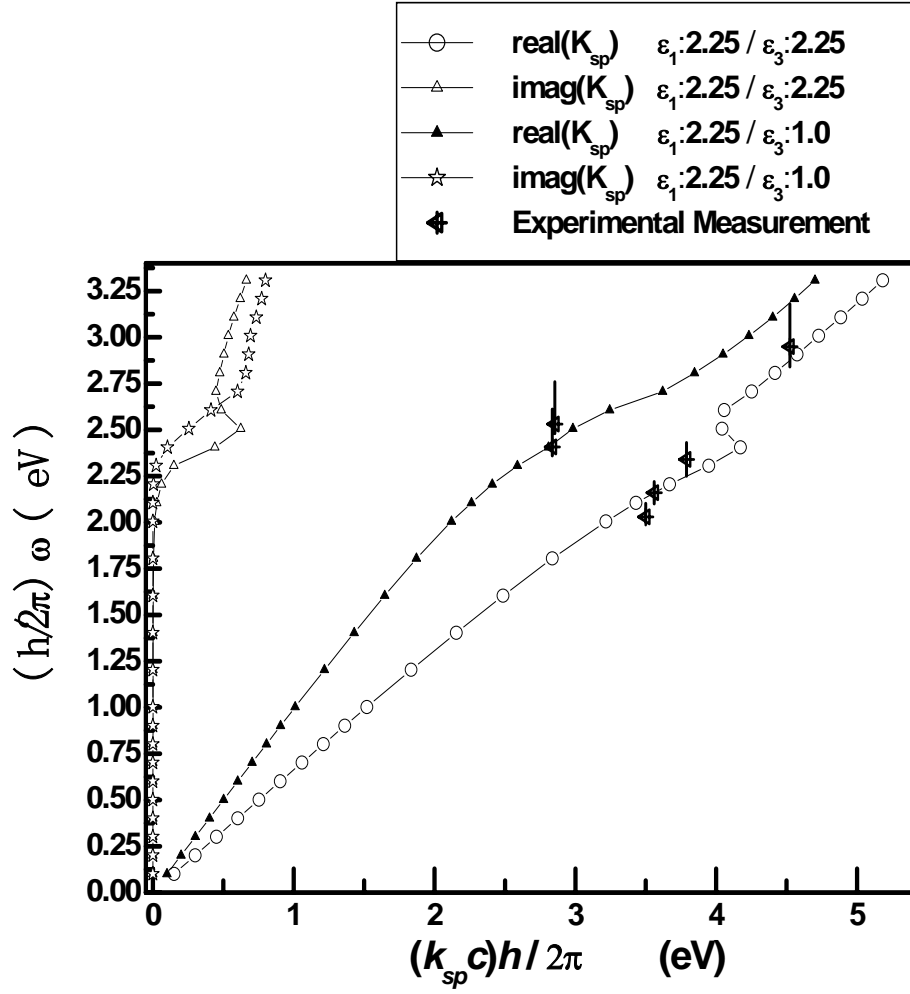


Figure 2.12: Dispersion relation of symmetrical fields and the experimental data fit.

Table 2 shows the fitting order.

$\lambda$ (nm)	$\omega$ (eV)	$k_{sp}$ (eV)	$N$
515	2.408	2.8361	1
490	2.5306	2.8545	1
420	2.95	4.523	-2

(a)

$\lambda$ (nm)	$\omega$ (eV)	$k_{sp}$ (eV)	$N$
610	2.03	3.5	1
575	2.16	3.56	1
530	2.34	3.79	-2

(b)

Table 2.2: The calculated  $k_{sp}$  in equation (13) for each peak wavelength (a) incident  $\theta = 8.5^\circ$  (b) incident  $\theta = 31^\circ$

The transmitted signals with their corresponding angles do not fit to a pure Fraunhofer diffraction picture ( $k_{OUT} = k_o \sin \theta \pm n\bar{G}$ ). The two incident angles 8.5° and 31° are arbitrarily chosen for maximum transmittance and convenience. The transmitted light is red shifted gradually when the incident angle increases. This effect fits well with the SPP excitation picture. The transmitted spectrum is broadened and always continuous when the incident angle increases. This means that the diffraction effects as well as SPPs are excited over a broad spectral range. Theoretical calculations similar to ours may also be seen in A.V.Kat's paper<sup>20</sup>. The fact that SPPs are excited not just at some fixed angle, but over a broad spectral range indicates that the SPPs at both boundaries are coupled to each other.

### *Application I: Light Concentrator and Coupling Device*<sup>21</sup>

Since the PMMA grating/Au/Glass can generate SPPs, the grating area can be viewed as a SPP generator. From Dr. Smolyaninov's experiment<sup>22</sup>, a parabolic droplet sitting on top of a gold film can magnify the object information carried by SPP waves, if the object is near the focal point. In this section, a reverse device is demonstrated. It is shown in Fig. 2.13. When the object is placed at region A, the magnified image is shown in region B. The reverse situation is when SPP waves are generated in region B, they will be focused near the focal point, continue propagating, and then get scattered at the boundary of the apex. The focusing effect has also been demonstrated previously<sup>21, 23 ~ 24</sup> and is shown in the following figures.

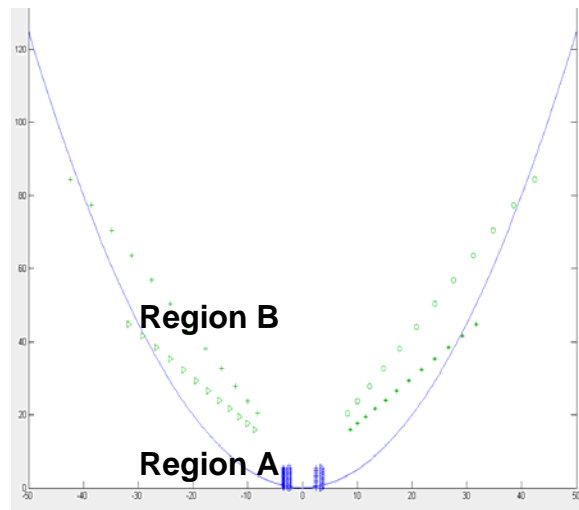


Figure 2.13: Geometric optics of a reflective-type parabolic lens. If the object is placed in region A, then the magnified image is formed in region B. If the object is located in region B, then the shrunk image is shown in region A.

A PMMA parabolic lens with size  $\sim 30 \mu\text{m}$  is patterned on top of an intact 50 nm thick

Au film. A bi-grating with 500 nm pitch is patterned, shown in Fig. 2.14 (a). The grey

spot near the apex is the focal point of this parabola. With illumination at the correct

angle, Fig. 2.14 (b) shows the field enhancement between the apex and the focal point.

When the incident power is strong and the coupling is efficient, we can even see the SPP

propagation trace shown in Fig. 2.14 (c).



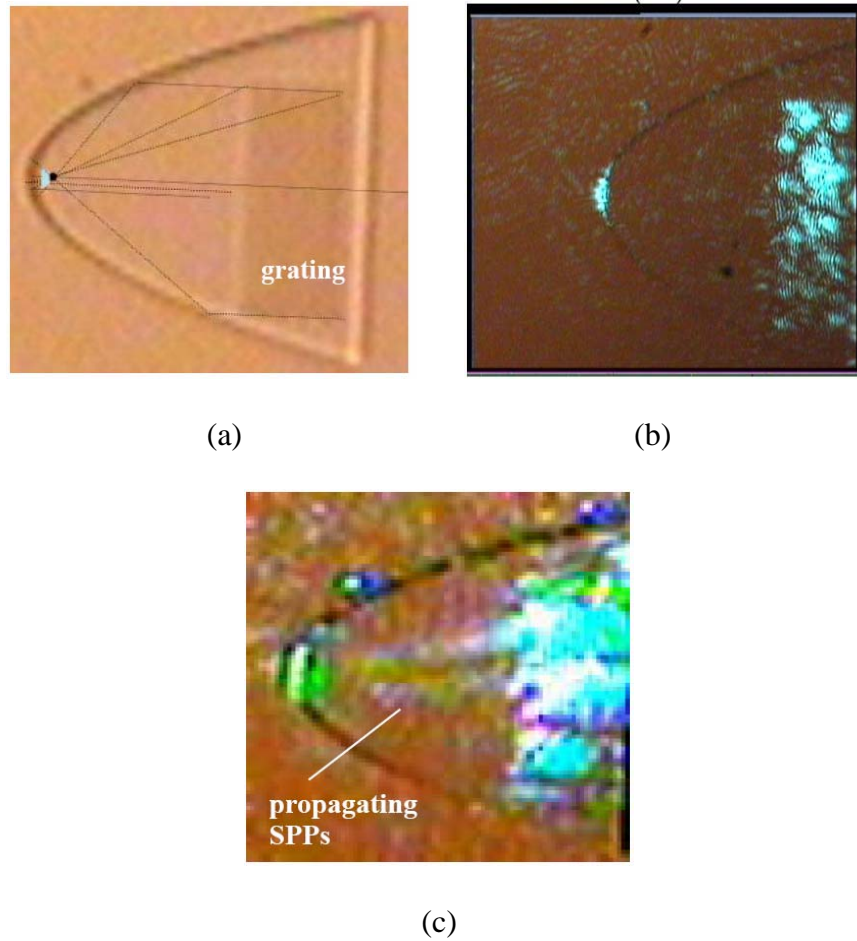


Figure 2.14: (a) Parabolic PMMA mirror with a rectangular bi-grating area formed inside. The grey trapezoid near the focus point of the parabola is the image of the rectangular bi-grating obtained using geometric optics (ray tracing). (b) After illuminating the bi-grating with 502 nm laser light, the field enhancement is observed between the apex and the focus of the parabola. (c) Optical energy propagation towards the apex may be visualized at the increased laser power due to Rayleigh scattering of the SPP field in the PMMA film.

Further, we demonstrated a parabolic lens with a waveguide attached to the apex point.

Fig. 2.15(a) and (b) show the focusing and guiding effect through a straight waveguide.

In (c) a curved waveguide with radius  $4 \mu\text{m}$  is shown and the guiding effect is strong.

Fig. 2.15 (d) shows the AFM image of the waveguide. The width of the waveguide is  $\sim$

200 nm and the height is  $\sim 138$  nm. We demonstrate here one way to couple light into plasmonic waveguides.

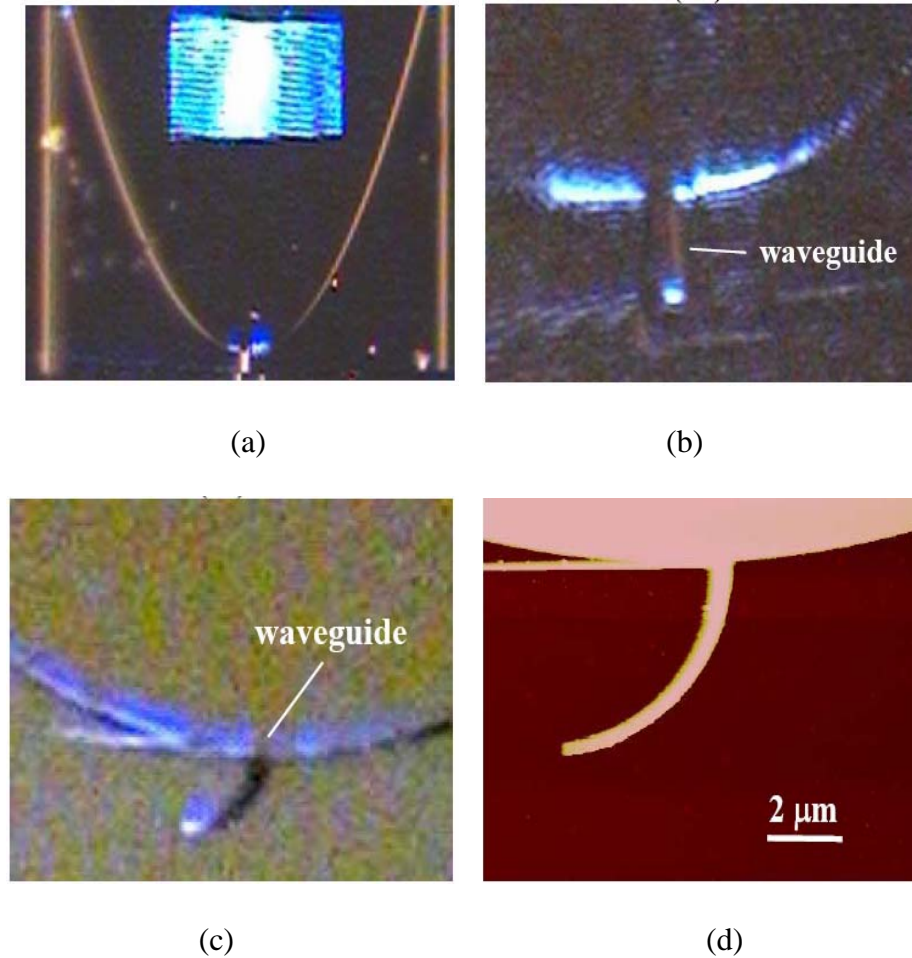


Figure 2.15: (a) Linear dielectric waveguide formed near the apex of the parabolic PMMA mirror. In (b) coupling and guiding of the optical energy down the end of the linear waveguide shown in (a) is demonstrated. (c) In a similar experiment, optical energy is coupled and guided down the curved dielectric waveguide. (d) AFM image of the curved waveguide formed at the apex of the parabolic mirror. The thin horizontal stripe of PMMA is used to scatter SPPs that may propagate through the mirror boundary.

One concern about the plasmonic structure is the attenuation length. The following simulation results show that SPP guiding through a long path is possible in our device structure. The modeling layer structure is shown in Fig. 2.16. With the continuity on the

boundaries, we can solve Maxwell's equations<sup>25</sup>. The propagation length is sensitive to the dielectric constant of gold. At  $\lambda=515$  nm, the dielectric constant is in a range with real part:  $-4 \sim -5$  and imaginary part:  $2j \sim 3j$ . The basic modes are symmetrical and anti-symmetrical fields. The symmetrical field has a longer propagation length than the anti-symmetrical field. When the PMMA layer is thick, a second mode appears and has a much longer propagation length than the first mode set. It is less lossy because there is more field distributed in the dielectric region than in the metal region. Fig. 2.17 shows the propagation length for different parameters. The length of our demonstrated parabolic device is about  $20 \mu\text{m}$ . It shows strongly that the second mode propagation is involved. With this coupling scheme, we will be able to implement some surface plasmonic circuits.

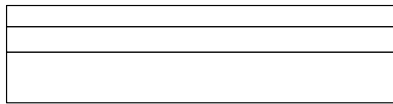
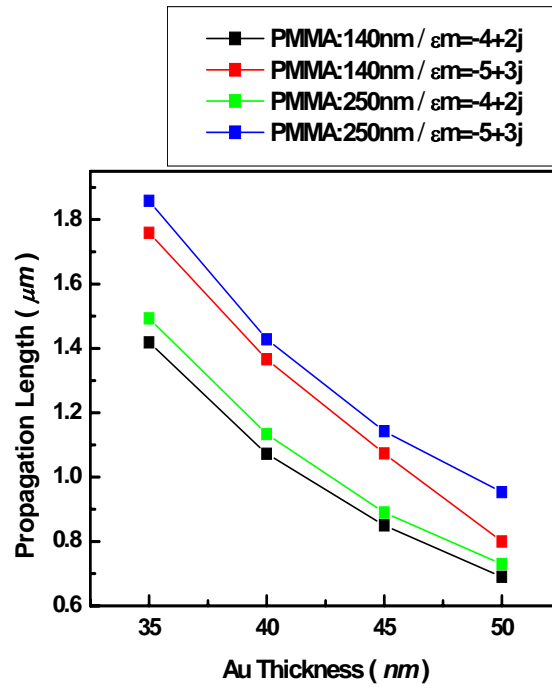
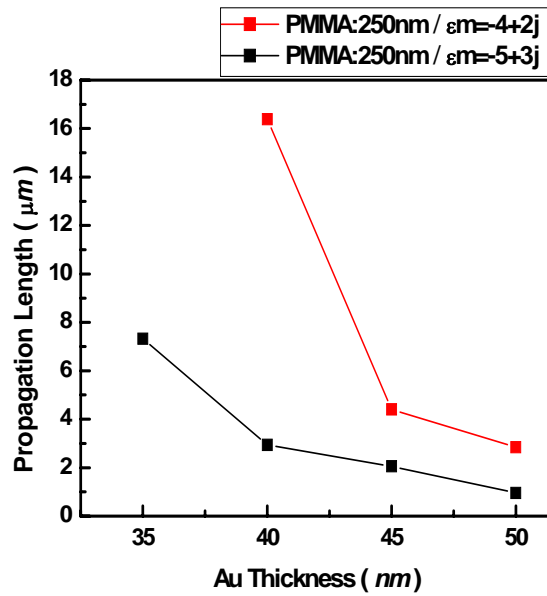


Figure 2.16: Structure used in simulation.



(a)



(b)

Figure 2.17: (a) Propagation length of the first symmetrical mode with PMMA thickness 140 nm and 250 nm respectively. (b) Propagation length of the second symmetrical mode with PMMA thickness 250 nm.

## *Application II: Nonlinear Signal Processing of Enhanced Transmission*

In another set of experiments a 50 nm thick gold film was sputtered onto chalcogenide glass, and a photo-induced grating was formed in the glass under the gold film in a conventional two-beam interference setup. Very high transmission of the photo-induced grating area has been observed by illuminating this area with a weak probe beam after the slow photo-induced recording process was complete<sup>26</sup>. The image of the transmission through the sample is shown in Fig. 2.18. Light transmission is blocked over most of the glass sample area because of the sputtered gold film. The bright spot near the center region appears where the photo-induced grating was formed. This effect demonstrates the possibility of all-optical signal processing using the enhanced light transmission phenomenon. However, in order to be practical, the chalcogenide glass ( $\text{As}_2\text{S}_3$ ) should be replaced with a fast nonlinear crystal.

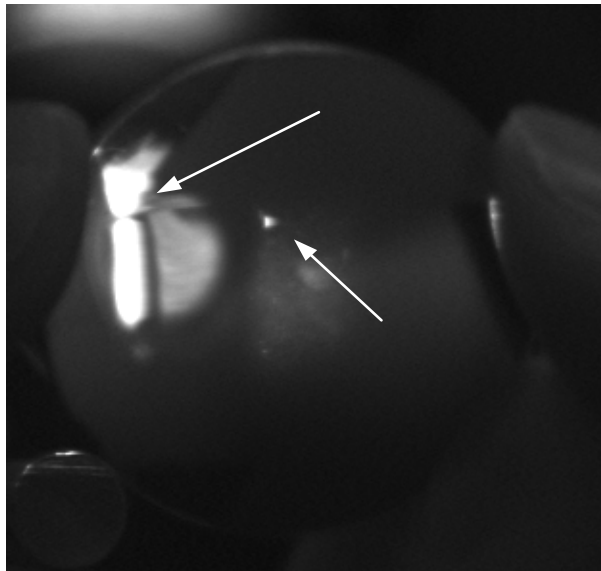


Figure 2.18: The image of light-induced resonant transmission through a continuous gold film on  $\text{As}_2\text{S}_3$  glass.

## **Chapter 3: Two-Dimensional Negative Refractive Index Device in the Optical Frequency Range**

### *Introduction to Left-Handed Materials*

Recent progress in nano-fabrication makes left-handed material or a negative index medium (NIM) possible. The first concept was discussed by Rayleigh in 1902 and a clear discussion goes back to 1968 from a Russian scientist Victor Veselago<sup>27</sup>. With negative electrical permittivity ( $\epsilon$ ) and magnetic permeability ( $\mu$ ), a so-called “left-handed material” (the  $k$  - wave vector,  $E$  - electric field and  $H$  - magnetic field form the left-handed vector relationship), a lot of unusual physical properties happen: 1. Phase and energy velocities are in opposite directions. 2. The Doppler Effect is reversed. 3. Snell’s law shows light bending into the other half plane. Following his speculative paper in 1968, Sir John Pendry from Imperial College, London, revisited the concept of a negative index material in 2000, and claimed that this negative material not only can reverse the phase properties of the incoming light, but can also amplify the evanescent components, which decay quickly in a regular medium. This provides a so-called “perfect lens,” which can form images beyond the diffraction limit<sup>11</sup>. Although this claim is controversial<sup>28~30</sup>, several of experiments have been reported and discussion continues. The following section aims to illustrate these ideas in a non-ambiguous way without any assumptions of negative permittivity and permeability. This chapter includes topics about two-dimensional negative refractive index devices and the demonstration of a “Superlens” with sub-wavelength image resolution.

## Characteristics of the Negative Refractive Effect

Isotropic Medium:

The definition of group velocity  $\overline{V}_g$  is as follows:

$$\overline{V}_g \equiv \nabla_{\vec{k}} \omega(\vec{k}) \quad (14)$$

$\vec{k}$  is the wave-vector and  $\omega(\vec{k})$  is the dispersion relation of the medium.

For isotropic and low loss media,  $\omega(\vec{k}) \equiv \omega(k)$  (15)

If  $\frac{d\omega(k)}{dk} < 0$ ,  $\overline{V}_g$  and  $\hat{k}$  will be point in opposite directions. And  $\hat{k}$  represents the

direction of  $\overline{V}_p$ , the phase velocity. So we can draw a conclusion that if  $\frac{d\omega(k)}{dk} < 0$ ,

then  $\hat{V}_g = -\hat{V}_p$ , which in the microwave world is described as a backward wave situation.

This can be seen in the SPP dispersion curve shown in Fig 3.1:

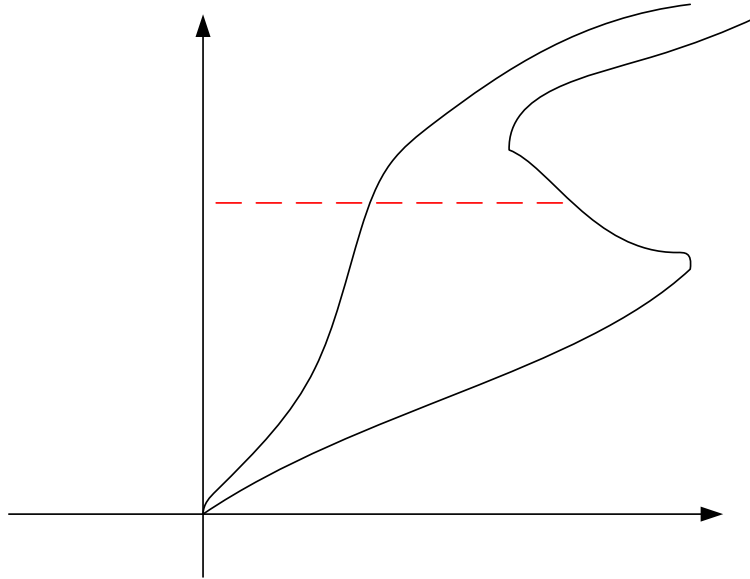


Figure 3.1: Dispersion relation of SPP on a gold/Glass semi-infinite interface.

$\hat{V}_g = -\hat{V}_p$  in Region II where  $\frac{d\omega(k)}{dk} < 0$ . Let's look at Snell's law operating at  $\omega_o$  between two different media that show the abnormal dispersion curve in Region II and also in the normal dispersion relation. Snell's law determines momentum conservation parallel to an interface as in the following equations, but doesn't impose any restriction on group velocity properties:  $n_1 \sin \theta_1 = n_2 \sin \theta_2 \Rightarrow k_1 \sin \theta_1 = k_2 \sin \theta_2 \Rightarrow k_1^{\parallel} = k_2^{\parallel}$ . The relation  $\hat{V}_g = -\hat{V}_p$  is determined by the definition of group velocity in the abnormal dispersion region. When the refraction picture is determined by applying Snell's law, momentum conservation and the backward wave behavior are two constraints. Fig. 3.2 shows two possible sets of refraction behavior that might occur at  $\omega_o$ . Assume that SPPs are incident from a normal optical medium I' and are refracted into an abnormal medium II'. Figs. 3.2 (a) and (b) are the correct depictions, while (c) and (d) violate the causality property because energy flows backwards towards the source. This can be a little bit confusing because the signs of  $V_p$  and  $V_g$  in Fig. 3.1 are not consistent with the intuitive vector signs in Fig. 3.2 (a) and (b). Here the dispersion  $k_{sp}$  vector is along the interface, so every concept discussed here should be related to in-plane components. With this point, the  $V_{p2}^{\parallel} > 0$  and  $V_{g2}^{\parallel} < 0$  shown in Fig. 3.2(a) and (b) are consistent with the conditions  $V_p > 0$  and  $V_g < 0$  shown in Fig. 3.1. Although the interface between I' and II' breaks the symmetry of the media, the directivity criterion derived from an assumption of isotropy should still be valid when light travels away from the interface.



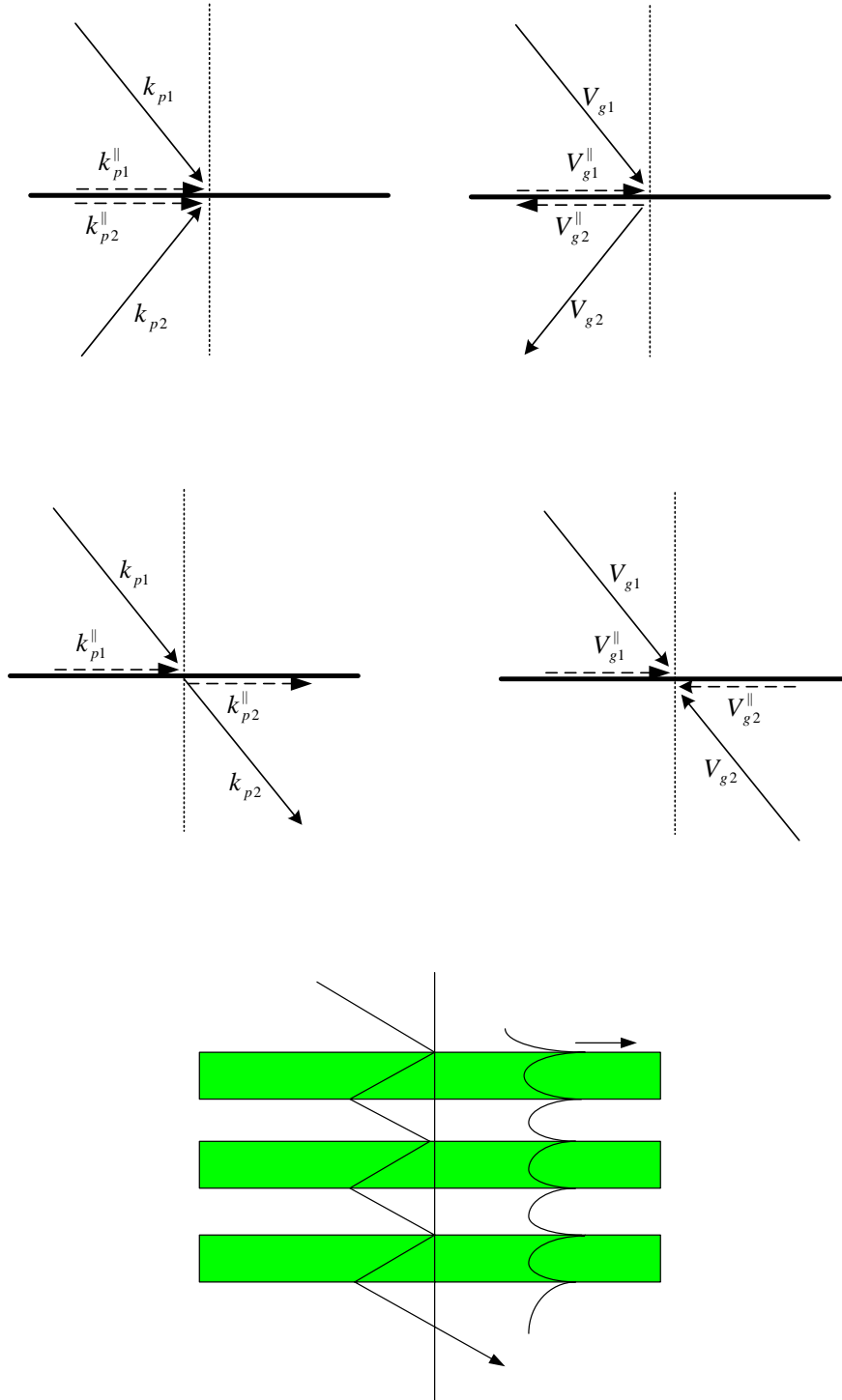


Figure 3.2: (a) negative refraction: momentum conservation. (b) Negative refraction: derived group velocity direction. (c) Positive refraction: momentum conservation. (d) Positive refraction: derived group velocity direction. (e) Correct refraction picture in a many-layered structure.

Let's look at the many-layered structure in Fig. 3.2 (e): The correct picture for SPP propagation between normal and abnormal dispersion regions is determined as previously and negative refraction is shown. The structure can be viewed as made up of locally isotropic media in alternating different layers. From the above discussion, the effective refractive index  $n$  in Region II is negative.

What happens to the wave-front evolution in a layer of negative refractive index  $n$  material? This can be explained using in Fig.3.3. Assume that TM laser light is focused at the interface between  $n_1$  and  $n_2$ . To determine the convergence direction of the wave front, the continuity of the tangential H field can be applied at the interface. The detailed explanation is as follows: in Fig. 3.3(a), the wave front of the refracted beam A2 and the reflected beam A1 at the first interface should be continuous. A1 is definitely divergent as it propagates out, so that A2 is divergent. Again, A3 is even more divergent which makes A4 divergent. In Fig. 3.3(b), with a layer of negative material, the picture is different. The wave front of B3 is continuous with that of B1 instead of B2. The wave front of B4 is continuous with that of B3 at the second interface. In this case, B4 converges again after passing through a layer of negative material. Naturally, light scattered from an object tends to diverge as it propagates out. However, in a negative layer, the phase of far-field components (the propagating light) can be reversed and the beam is then convergent on the image plane. This indicates that more far-field components can be collected at the image plane which results in a better image quality.

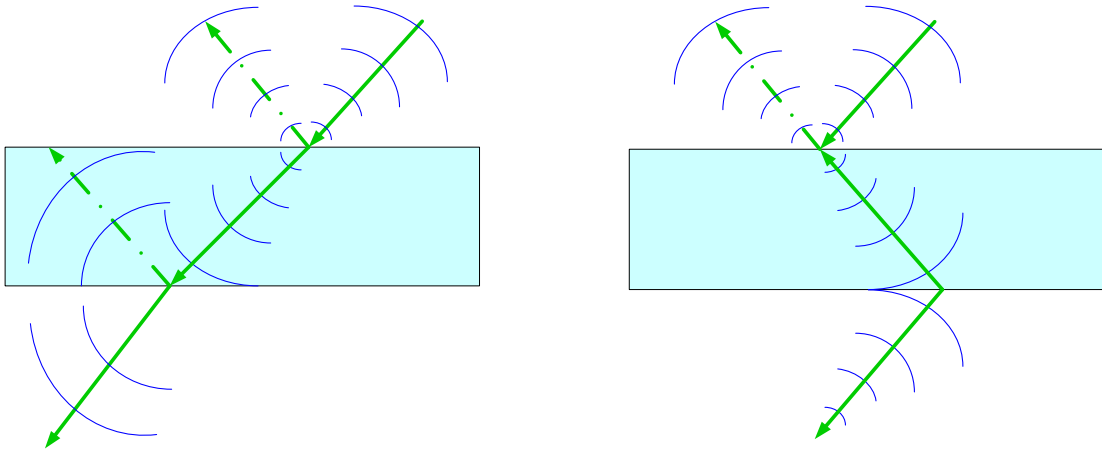


Figure 3.3: Wave front alternation in a three layered structure: the incident wave is focused on the upper interface and the outgoing wave in  $n_3$  is different due to different  $n_2$  polarity (a) For  $n_2 > 0$ , the wave diverges in  $n_3$  medium (b) for  $n_2 < 0$ , the wave focuses again in the  $n_3$  medium.

A1

The other interesting characteristic of a negative refractive index is that evanescent waves can be amplified instead of attenuated. Although mathematically this is correct, in reality the real behavior of SPP waves must be included. For a three layered structure with a metal layer in between, as shown in Fig. 3.3(b), the ratio between the output surface plasmon E field at the  $n_2/n_3$  interface and the incident field at the  $n_1/n_2$  interface can be larger than 1, which means that the field is enhanced. With a pure bulk material, there is no negative refraction if no loss is involved<sup>31</sup>. Therefore, Pendry's statement on the amplification of evanescent waves is correct when SPP modes are involved or the negative material occupies an extremely small volume, which is described in the following section – an anisotropic medium. Recently, several groups have demonstrated negative  $\epsilon$  and negative  $\mu$  with the intention of decreasing loss in the optical frequency range<sup>32-34</sup>. With both negative  $\epsilon$  and  $\mu$ , no imaging work beyond diffraction limit has been demonstrated. The elimination of loss is still the main issue.

A3

A2

A4

Anisotropic Medium:

In 2006, it was pointed out by Narimanov<sup>35</sup> and Engheta<sup>36</sup> that without both negative  $\varepsilon$  and  $\mu$ , sub-wavelength imaging can still be implemented. This forms another perspective on the so-called “Hyperlens” effect. Their models show that with layered anisotropic materials [ $\varepsilon_{\parallel} < 0, \varepsilon_{\perp} > 0$ ] or [ $\varepsilon_r < 0, \varepsilon_{\phi} > 0$ ] (or the other way round), sub-wavelength imaging below the diffraction limit ( $\lambda/3$ ) can be displayed. It can be described as follows<sup>35</sup>. In polar coordinate, the normal dispersion curve of light traveling in a regular medium is

$$k_r^2 + k_{\theta}^2 = \varepsilon \frac{\omega^2}{c^2} \quad \text{or} \quad \frac{k_r^2}{\varepsilon_{\theta}} + \frac{k_{\theta}^2}{\varepsilon_r} = \frac{\omega^2}{c^2}$$

But if we have a layered medium, the dielectric constant can be defined effectively as

$$\varepsilon_{\theta} = \frac{\varepsilon_m + \varepsilon_d}{2} \quad \text{set } > 0 \quad (\varepsilon_m + \varepsilon_d > 0)$$

$$\text{and } \varepsilon_r = \frac{2\varepsilon_m\varepsilon_d}{\varepsilon_m + \varepsilon_d} \quad \text{set } < 0 \quad (\varepsilon_m \cdot \varepsilon_d < 0)$$

$$\Rightarrow \frac{k_r^2}{\varepsilon_{\theta}} - \frac{k_{\theta}^2}{|\varepsilon_r|} = \frac{\omega^2}{c^2}$$

So the dispersion curve can be plotted as shown in Fig 3.4. So for a given frequency  $\omega$ ,

$k_r \uparrow, k_{\theta} \uparrow$ : there is no limit to how large these wavevector components can become.

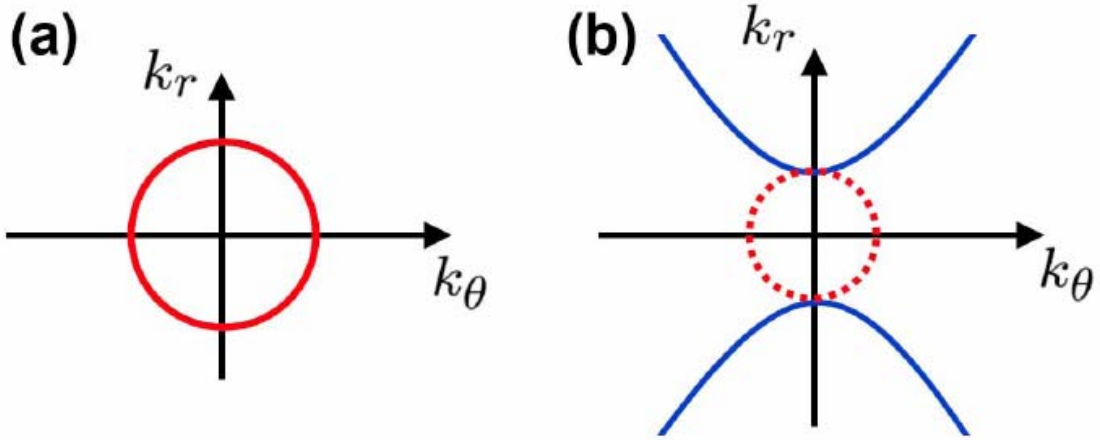


Figure 3.4: Dispersion relation for isotropic medium (a) and for a material with  $\epsilon_r < 0, \epsilon_\theta > 0$  (b). Note that for a fixed frequency, the wave vector  $k$  can take on arbitrarily large values (within the effective medium approximation).

Because  $k_\theta r = m$  (angular momentum), for a given  $m$ ,  $r$  is very small,  $k_\theta$  is very large. In regular dispersion,  $k_r$  is imaginary if  $k_\theta$  is larger than a certain value. However, in a layered medium,  $k_r$  can exist.

In this theory:  $\frac{k_r^2}{\epsilon_\theta} - \frac{k_\theta^2}{|\epsilon_r|} = \frac{\omega^2}{c^2} \approx k_{xy}^2 - k_z^2 = \frac{\omega^2}{c^2}$ , which is a dispersion of the SPP at the

interface between a metal and a dielectric. It can be further expressed as

$$\begin{cases} k_{sp}^2 + k_{z1}^2 = k_1^2 = k_o^2 \epsilon_m \\ k_{sp}^2 + k_{z2}^2 = k_2^2 = k_o^2 \epsilon_d \end{cases} \quad \text{where } k_{sp}^2 > 0, k_{z1}^2 < 0, k_{z2}^2 < 0.$$

Previous authors<sup>35</sup> view the finely-layered structure as a high order mode supporter. In  $\hat{r}, \hat{\theta}$  both modes are propagating, while for SPPs at the interface,  $k_{sp}$  is propagating while  $k_z$  is non-propagating. In the layered structure, only the hyperbolic dispersion is involved. This is similar to SPP propagation with short effective wavelength with  $k_{sp}$  superluminal, which means  $k_{sp}$  is larger than light. In Narimanov's and Enghta's pictures, no loss ever

needs to be included. So the hyperbolic dispersion model represents an old point of view. If the medium is isotropic, metal loss is the origin of the abnormal dispersion, which results in negative refraction and phase compensation effects.

### *Dispersion Relation of Dielectric/Gold/Dielectric Structure*

To better understand devices to be described shortly, the dispersion relations are simulated using two kinds of three-layered structures: Air/Gold (50 nm)/Glass and PMMA/Gold (50 nm)/Glass. Symmetrical and anti-symmetrical fields are the two eigen fields shown in Fig 3.5. The dispersion relations of the two eigen fields are shown in Fig 3.6 and 3.7, respectively.

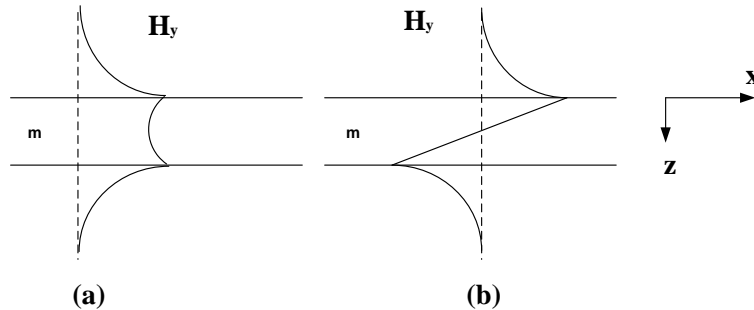


Figure 3.5: Field distribution of symmetric and anti-symmetric SPP modes on a thin metal film.

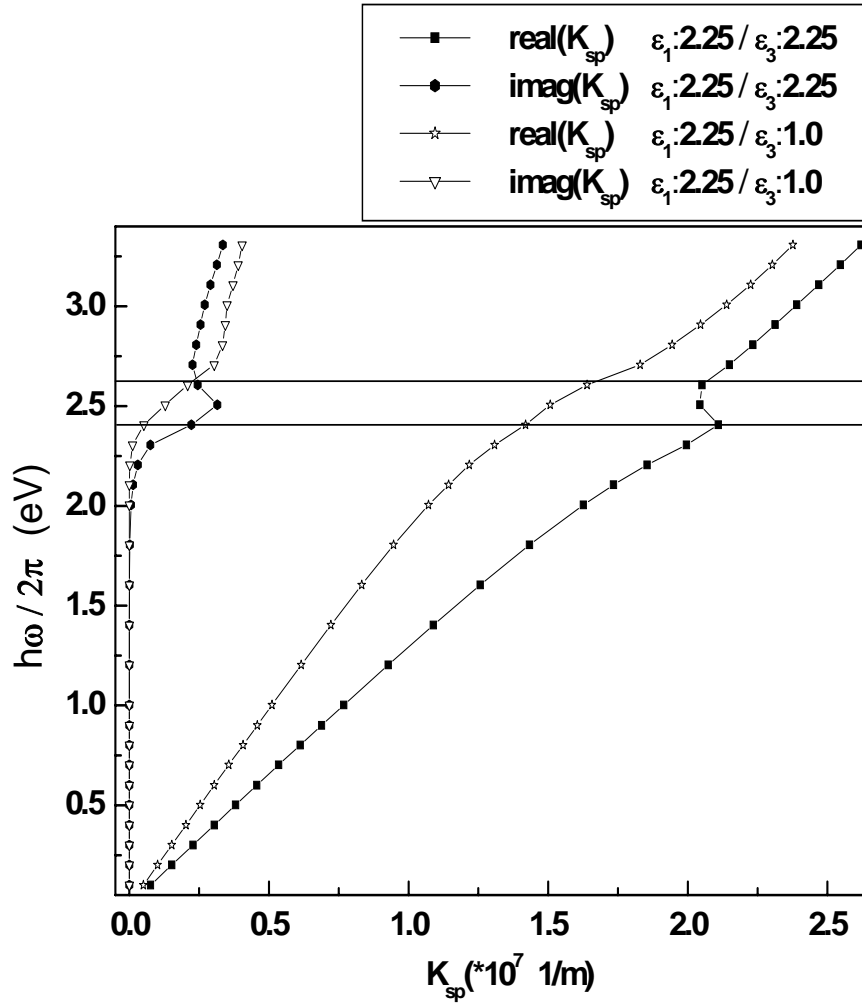


Figure 3.6: Dispersion relation of Symmetrical modes on two three-layered structures.

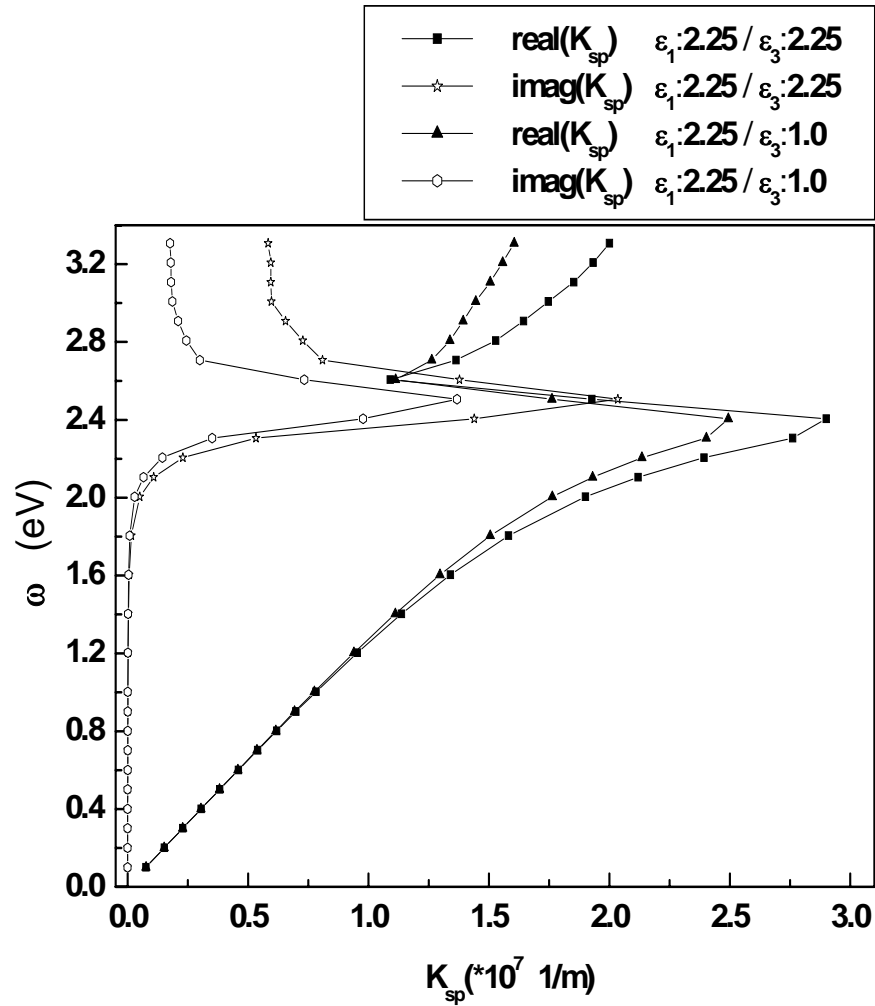


Figure 3.7: Dispersion relation of Symmetrical mode on two three-layered structures.

The symmetrical field on Air/Gold (50 nm)/Glass is normally-dispersive in the interesting frequency range marked between the two red lines while on the PMMA/Gold (50 nm)/Glass structure the field possesses negative refractive index behavior (phase velocity and group velocity have the opposite signs). With the positive and negative refractive layer design, a lot of interesting devices can be demonstrated. The anti-symmetrical fields on both three layered structures attenuate quickly. Therefore, the anti-symmetrical fields



don't play a role. Snell's law provides a simplified picture of what is happening, and is applied in my analysis. It helps to understand the device behavior.

A similar concept utilizing the negative mode behavior of planar SPPs have been discussed in Lezec et al.'s paper in Science Express<sup>37</sup>. They used a Metal/Insulator/Metal structure (Ag/Si<sub>3</sub>N<sub>4</sub>/Ag and Au/Si<sub>3</sub>N<sub>4</sub>/Ag) to demonstrate that there is a wavelength region where phase velocity and group velocity are oppositely directed. They measured the refraction angle and state that from 470 nm to 530 nm, the Au/Si<sub>3</sub>N<sub>4</sub>/Ag planar waveguide structure shows the negative refraction effect. The advantage of their demonstration is that there is no periodic grating structure so that the results don't show any ambiguity between diffraction and real negative refraction effects. A different but similar trick is to play with the mode dispersion curve in waveguide structures. It was demonstrated with an abnormal mode dispersion curve, and negative refraction can be found as well<sup>38, 39</sup>.

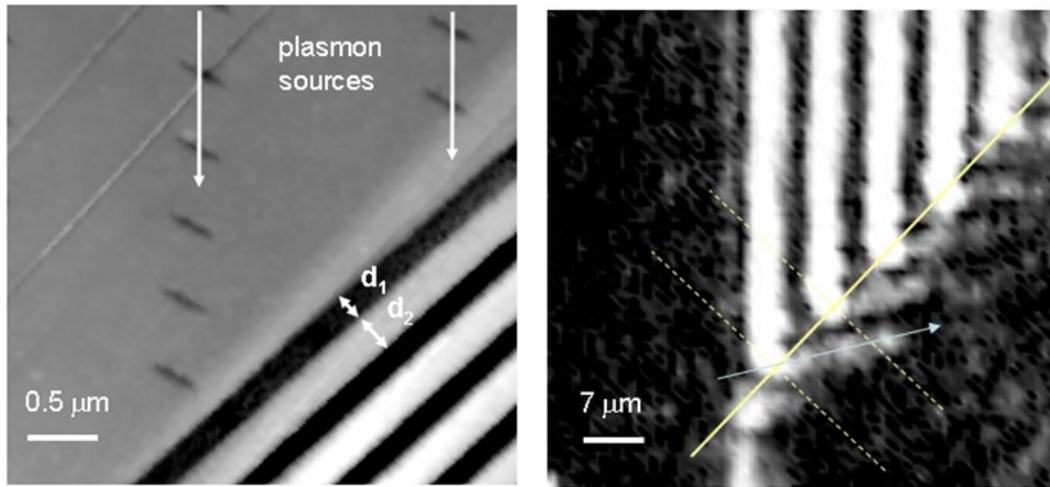
### *Experimental Evidence of a Negative Refractive Index*

The following examples are to demonstrate the negative refraction effect in various device structures. The beam propagation length in the following pictures is approximately in the range of 10  $\mu\text{m}$ . Energy flows out and decays gradually.

#### *Snell's Law with Negative Refraction*

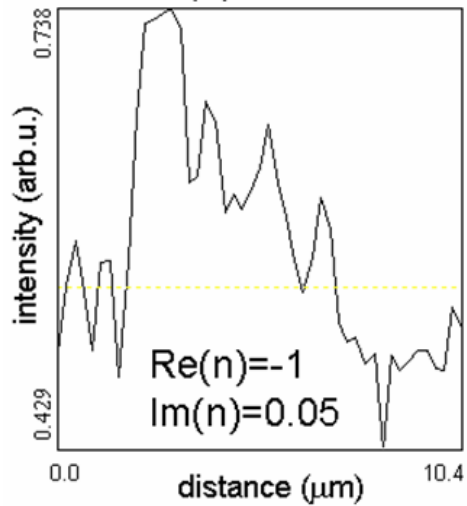
The AFM image of the device is shown in Fig 3.8 (a). A row of 500 nm periodic dots are placed at 45° near a set of stripe gratings with 500 nm periodicity as well. SPP waves are

generated by the dots and propagate into the periodic stripe grating region. The negative refraction effect is shown in Fig 3.8 (b). Using Snell's law  $n_1 \sin \theta_1 = n_2 \sin \theta_2$   $n_2$  can be estimated as -1 since both  $\theta_1$  and  $\theta_2$  are  $45^\circ$ .



(a)

(b)



(c)

Figure 3.8: (a) AFM image of the structure: The SPP wave propagates into the grating region at  $\theta = 45^\circ$ . (b) Optical image taken under a microscope. (c) The intensity analysis of one propagation beam.

### *Focusing Effect with Concentric Rings*

An interesting focusing phenomenon has been observed with the concentric ring stack in Fig 3.9. The AFM images of the concentric ring structure are shown in Fig 3.10 and 3.11. The periodicity of the ring stack is about  $0.83 \mu\text{m}$ . The widths between the PMMA/Gold ( $d_1$ ) and Air/Gold ( $d_2$ ) are important for this focusing effect. When  $n_1 d_1 = n_2 d_2$ , a balanced situation, the spot is tightly focused; when  $n_1 d_1 \neq n_2 d_2$ , the unbalanced condition, the beam does not converge efficiently. Fig 3.12 shows the unbalanced situation, in which case the focusing spot on the  $0.5 \mu\text{m}$  periodicity rings is not clearly seen.

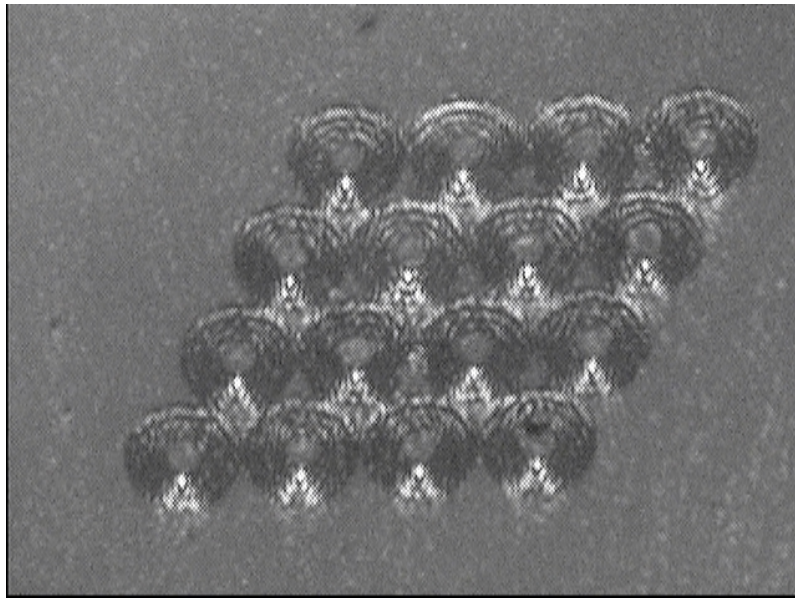


Figure 3.9: incident angle  $40^\circ$   $\lambda = 488\text{nm}$

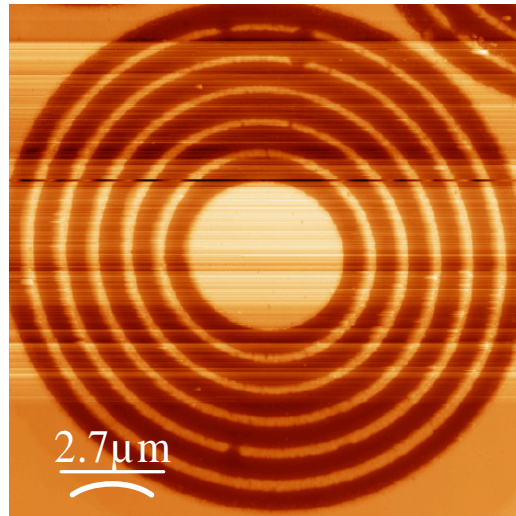


Figure 3.10: AFM image of the concentric rings.

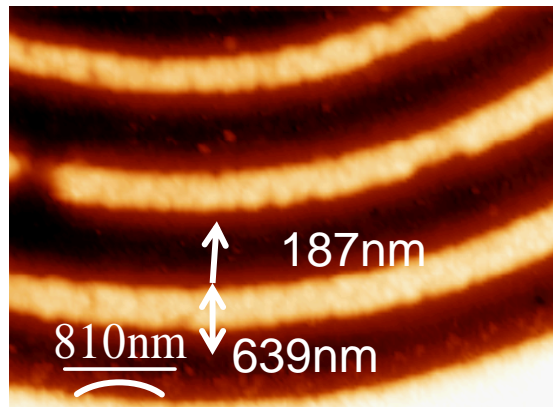


Figure 3.11: AFM image of the rings

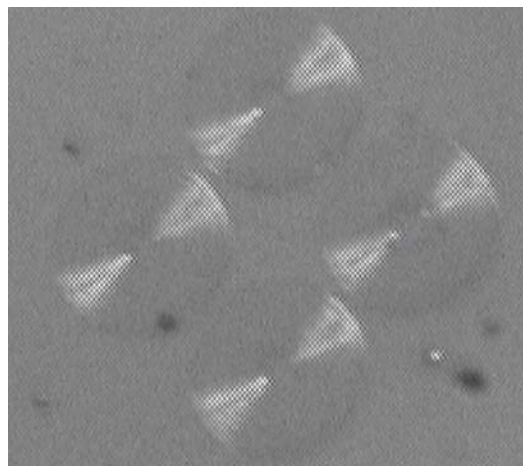


Figure 3.12: 488 nm unbalanced case

In our devices, propagation of two-dimensional SPP waves at the two-dimensional interface make the definition of  $\varepsilon$  and  $\mu$  rather difficult. The distance between each layer (each stripe) is 500 nm in our structure, which is much larger than in the effective anisotropic devices proposed by Narimanov. To really simulate the device, multiple scattering of SPPs between the many layered concentric rings may provide a more complete answer. From the focusing picture shown in Fig. 3.9, it was found that a “negative refractive index” is unavoidable in this situation.

In order to understand the focusing phenomena, ray-tracing has been adopted and the simulation structure is shown in Fig. 3.14. Alternating concentric layers shown in Fig. 3.13 with  $n_1$  and  $n_2$  are simulated. The thickness of each layer is 0.5  $\mu\text{m}$ . The inner and outer radii are 4  $\mu\text{m}$  and 14  $\mu\text{m}$ , respectively. Incident angle  $\theta$  defined on the plane is from  $0^\circ$  to  $50^\circ$ . The results are shown in polar coordinates. Rays stop at inner circle with  $r = 4 \mu\text{m}$ . From Fig. 3.14 (a) and (b), we know that if  $n_1$  and  $n_2$  have the same sign, the rays won't converge towards the center. The spots with  $\theta = 30^\circ, 40^\circ, 50^\circ$  in Fig. 3.14 (b) mean total reflection. No further ray path can be developed. However, if  $n_1$  and  $n_2$  have opposite signs, Fig. 3.14 (c) to (e) shows that the rays will go towards the center of the circle. When  $n_1 = -n_2$ , every ray will zig zag in the radial direction as shown in (c). The rays shown in Fig.3.14 (e) are over-focused. This simulation gives us a general picture of the necessity of adopting the concept of a negative refractive index in this structure.

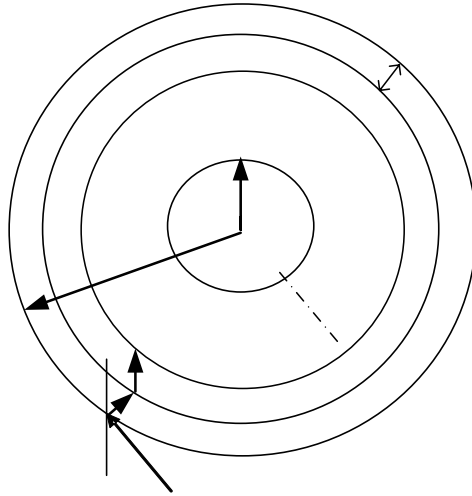


Figure 3.13: the simulation structure with  $\theta = 0^\circ, 10^\circ, 20^\circ, 30^\circ, 40^\circ, 50^\circ$ .

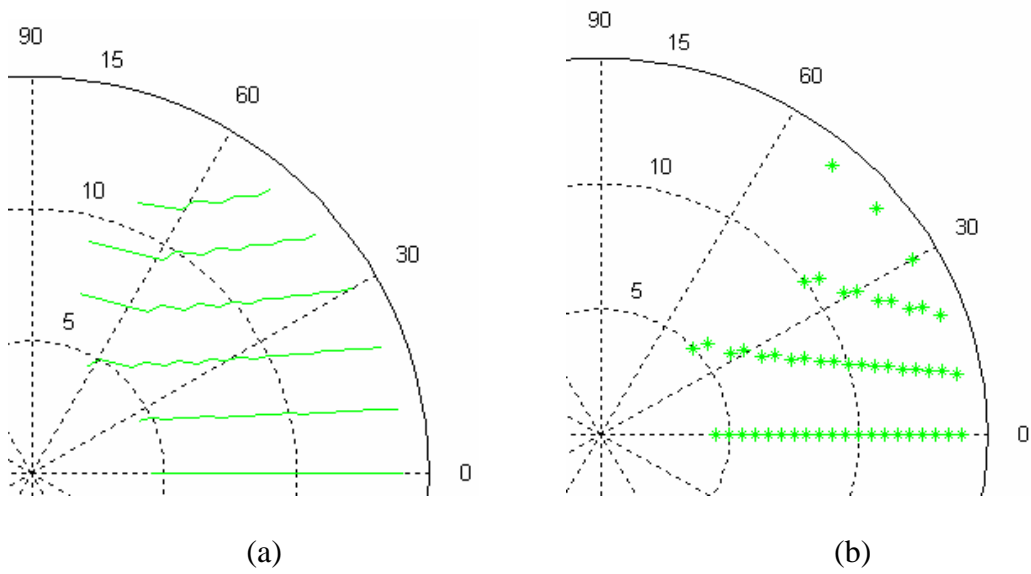


Figure 3.14: (a)  $n_1/n_2=1/2$  – less dense medium to dense medium. (b)  $n_1/n_2=2/1$  -- dense medium to less dense medium. (Spots at  $30^\circ, 40^\circ$  and  $50^\circ$  mean that total reflection occurred at the spot.)

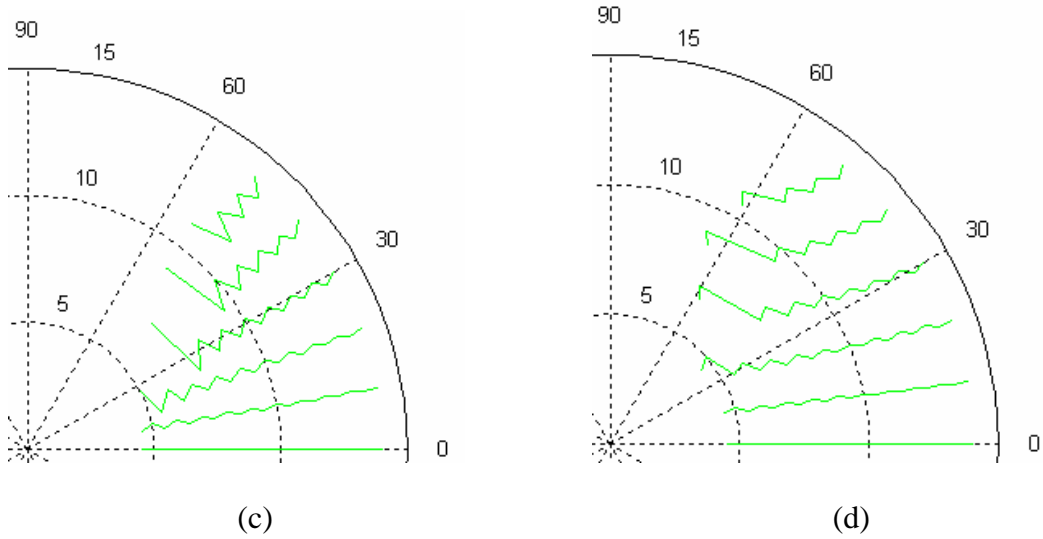


Figure 3.14: (c) Balanced case:  $n_1/n_2=1/(-1)$  -- positive medium to negative medium. (Rays at  $30^\circ$ ,  $40^\circ$  and  $50^\circ$  stop at where total reflection occurred.) (d)  $n_1/n_2=1/(-2)$  -- positive medium to dense negative medium.

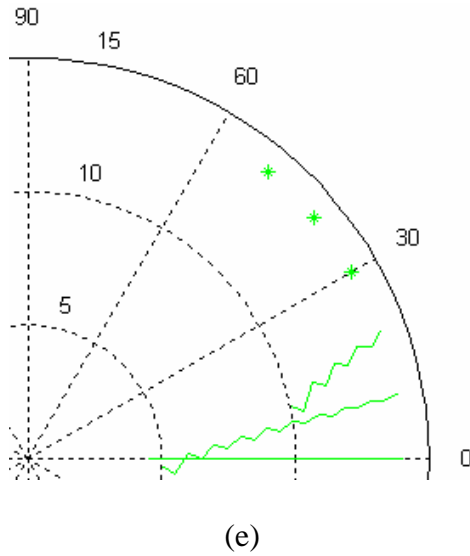


Figure 3.14: (e) Over focused case:  $n_1/n_2=2/(-1)$  -- dense positive medium to negative medium.

### *Magnifying Superlens in the Visible Frequency Range*

With positive and negative inter-layers shown in the previous section, an imaging device with sub-wavelength resolution can be demonstrated. Although our structure is similar to

Narimanov’s device design, we actually developed the concept independently. The demonstration of the device function is shown in Fig. 3.15. Three rows of dots are patterned in the center of the half circle gratings. 532 nm laser light is incident along the y axis at some elevation angle so that SPP on the three rows of dots can be excited under the phase matching condition. The alternating layers, the so called “superlens”, carry the sub-wavelength information to the outer rim. The scattered spots on the outer rim are discernible under a far-field optical microscope. Fig. 3.16 (a) shows the optical image of half-circle grating structure with three rows of dots in the center. The AFM image is shown in Fig. 3.16 (b) which is distorted a little due to the x-y scan asymmetry of the AFM machine. Dot spacing along x axis is fixed at 500 nm while row spacing along the y axis is varied in order to test the resolution. Row spacings of 500 nm (3 rows), 300 nm (3 rows) and 130 nm (2 rows) are shown in Figs. 3.16 (d) to (e).

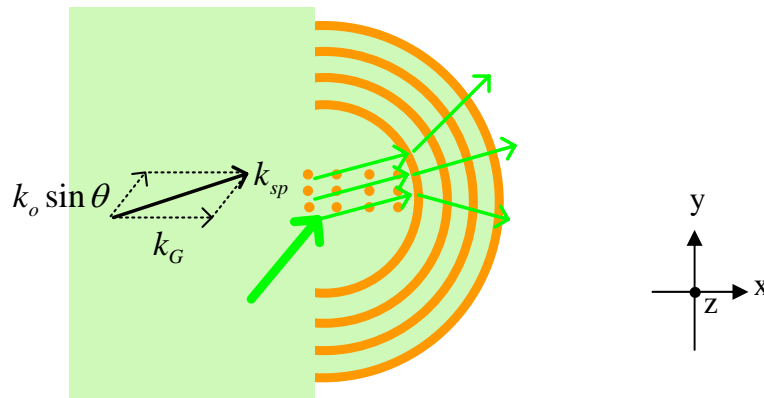
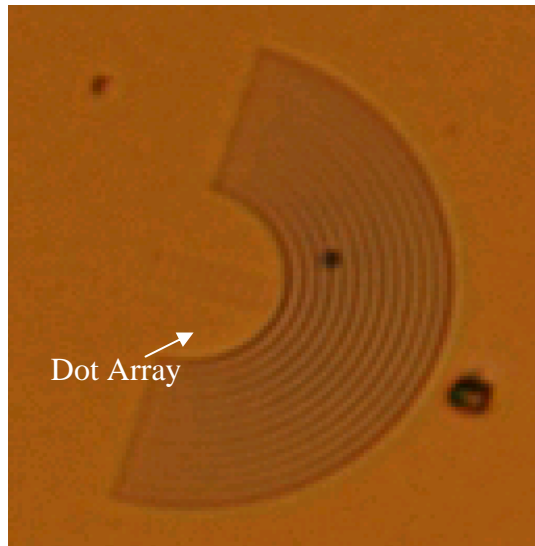
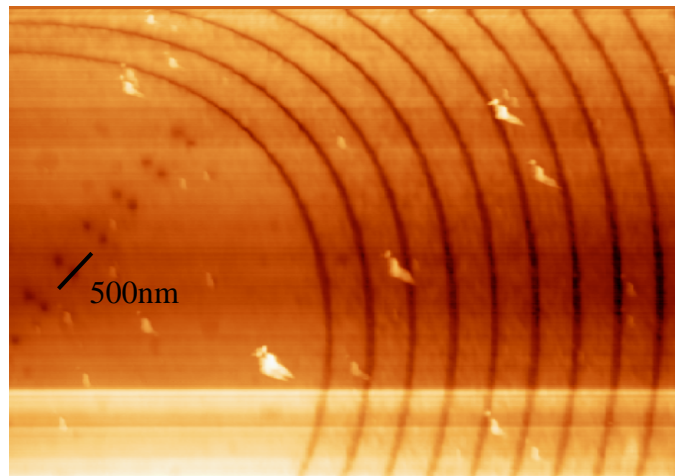


Figure 3.15: phase matching condition on the half-ring device





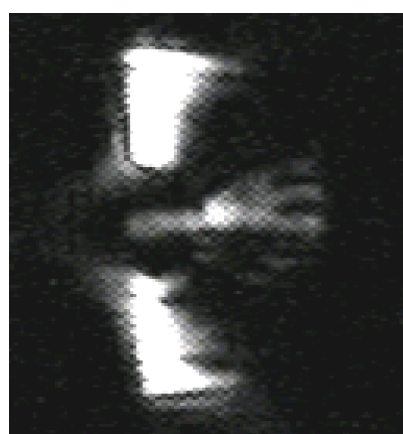
(a)



(b)



(c)



(d)



(e)

Figure 3.16: Image expansion effect with 532 nm laser: (a) optical microscope image (b) AFM image (c) 500 nm row spacing - 3 rows (d) 300 nm row spacing - 3 rows (e) 130 nm row spacing - 2 rows.

Fig 3.17 shows that the existence of the dots actually creates the outgoing rays. The question naturally arises: what makes the two directional beams in the center keep their high spatial frequency components (evanescent waves) as they propagate out through the half-ring gratings? Narimanov and Engheta discussed that the highly anisotropic structures that possess a hyperbolic dispersion relation can transmit high spatial frequency components without much loss. However, our device structure is partially anisotropic which can be seen in Fig 3.16(b). The air/Au gap is narrow compared to the PMMA/Au stripe region. The periodicity of the rings is  $0.5 \mu\text{m}$ . When the pitch is 400 nm or 300 nm, there is no such beam propagation effect. The  $0.5 \mu\text{m}$  periodicity is an important parameter in the beam scattering process. The beam which carries sub-wavelength information has to be coupled out to be perceived by us. So periodicity has to match the plasmon k-vector. Because our structure is a two-dimensional device, it is much harder to define the correct effective permittivity along the 2-D coordinates. What can be said in this picture is that the nature of beam divergence from the two or three

small beams is somewhat balanced while the beams are propagating through negative and positive index layers in the 2-D circular plasmonic crystal. Fig. 3.18 shows the resolution of our Superlens structure. The FWHM of the dot in the AFM image is 76.5 nm, while the optical beam width is around 61 nm. We can say that the current limitation results from fabrication precision. Except for the imaging function, the Superlens can be a coupler in a plasmonic circuit system. After signals are processed on various nano-scale devices in the center region, the results can be magnified and detected by a fiber probe at the outer rim. A 3-D multilayer hyperlens has been demonstrated by Zhang's group from Berkeley<sup>40</sup>. They can resolve a gap width of less than 200 nm.

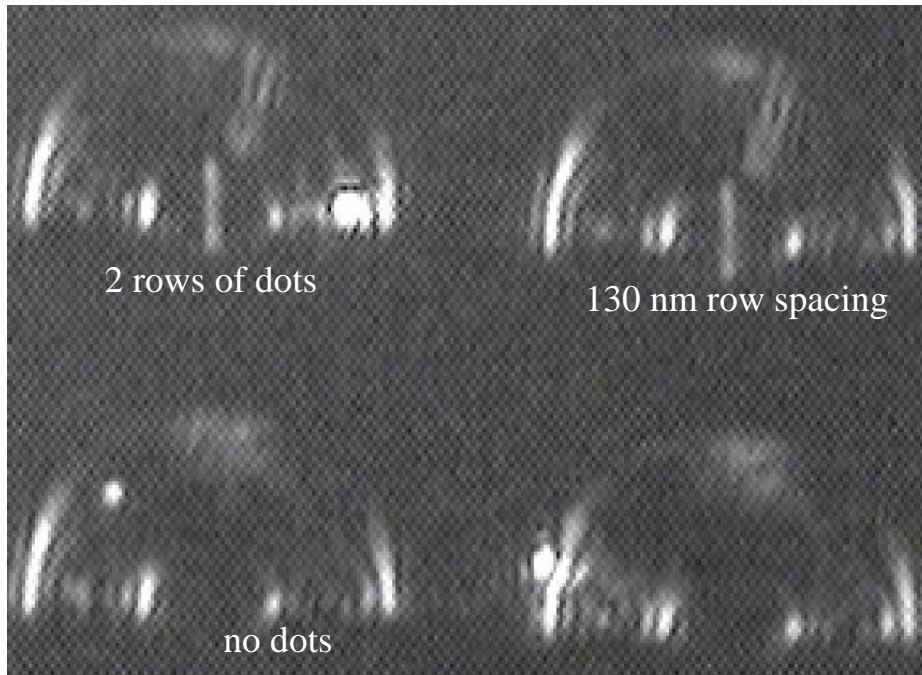
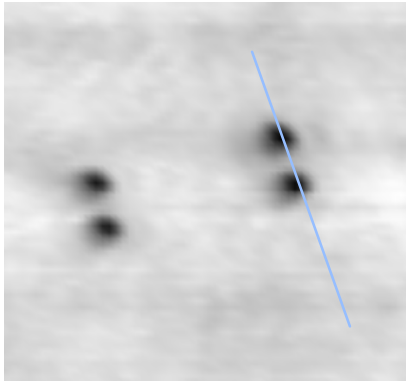
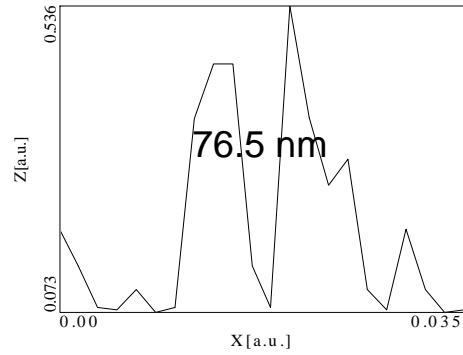


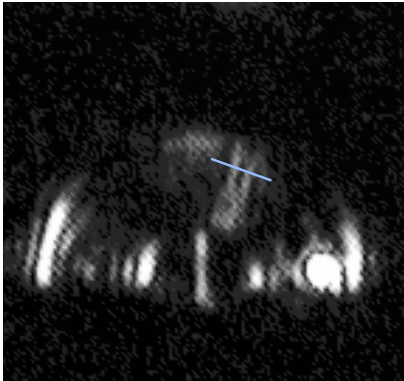
Figure 3.17: A comparison between two rows of dots in the center region and no array in the center.



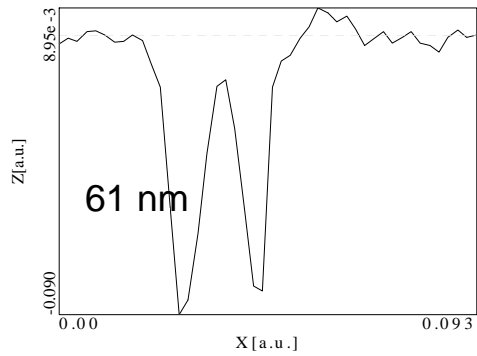
( a )



( b )



( c )



( d )

Figure 3.18: Resolution analysis (a) AFM image of two nano dots. (b) Cross section width of the dot is 76.5 nm. (c) Optical image of the dots magnified by the superlens device (d) the FWHM of the propagating beam is 61 nm.

It seems clear that the highly-anisotropic layered medium can support high angular modes at the circle center and circular gratings direct and magnify the beams as  $r$  increases. But the hyperbolic dispersion is not the dominant picture in these experiments. Negative refraction discussed in the isotropic medium is the main reason that the subwavelength images can be resolved by the layered structure when metal loss is included. The phase is balanced back and forth through Air/Au and PMMA/Au grating

stripes. In other words, if the operating wavelength is located in the normal dispersion region, say 632 nm, the subwavelength imaging will depend on the SPP short effective wavelength property, similar to Narimaninov's hyperlens principle. As for the resolution capability compared between SPP waves and a negative refractive lens (with loss mechanisms is included), negative refractive lens should have higher resolution because of its collectivity of spatial frequency components. A negative refractive material can maintain the evanescent components scattered from the object and transmit them while SPPs at short effective wavelength are still limited by diffraction.

### *Interference Effect in Two Focusing Devices*

Fig. 3.19 shows two sets of mirrored parabolic stacks with inner focal length  $10\ \mu\text{m}$  and outer focal length  $15\ \mu\text{m}$ . Each parabolic curve has the same focal point with focal length difference  $0.5\ \mu\text{m}$ . The distances between the centers of the two inner parabolas are  $9.7\ \mu\text{m}$  (left) and  $10.3\ \mu\text{m}$  (right), respectively.  $532\ \text{nm}$  laser light is incident from top and phase-matched. In addition to the focusing effect, clear constructive and destructive interference effects are seen.

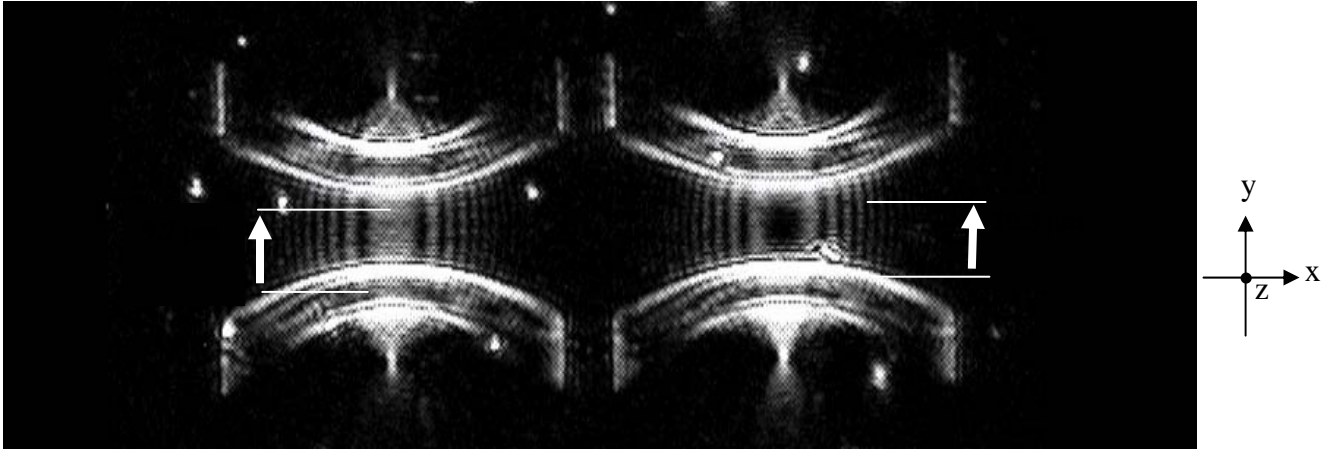
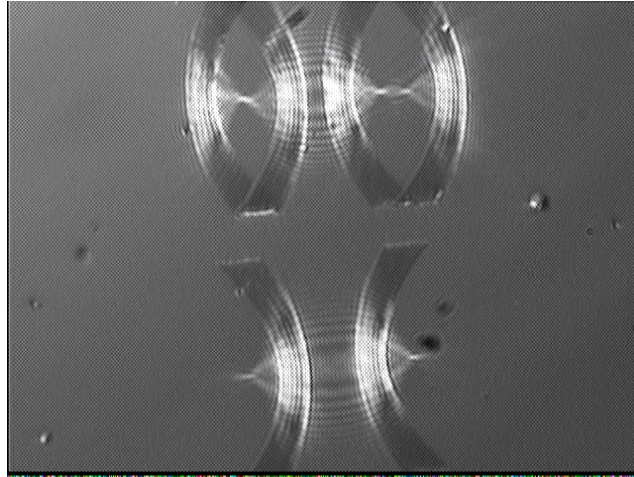
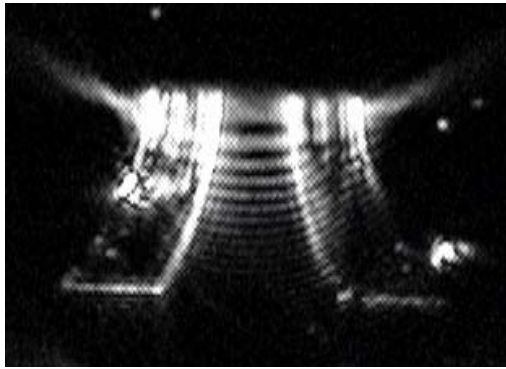


Figure 3.19: Con-focal parabolic gratings with inner focal length  $10 \mu\text{m}$ .

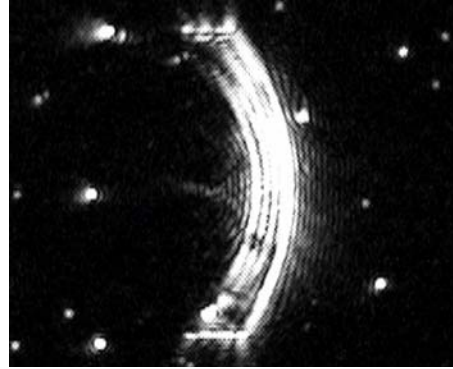
In order to check the coupling effect, more designs have been studied as shown in Fig. 3.20. The cavities formed by two parabolic gratings with different arrangements show different behavior. A concave cavity in Fig.3.20 (a) shows the coupling effect, while two gratings with a convex cavity don't seem to correlate to each other. Fig. 3.20 (b) shows if the grating cavity is halved, see Fig. 3.20(b), the pattern still exists. Energy doesn't seem to travel in a circular path in the cavity. This appears to be mainly a multi-layer scattering effect. Fig. 3.20 (c) shows that interference can't be formed in only one parabolic grating. While Fig. 3.20 (d) shows that without a multi-layer structure, the parabolic boundaries alone won't cause fringing effects. The negative refractive index in the grating region definitely plays a role in this abnormal phenomenon. However, to get a precise simulation, the FDTD methods will be needed.



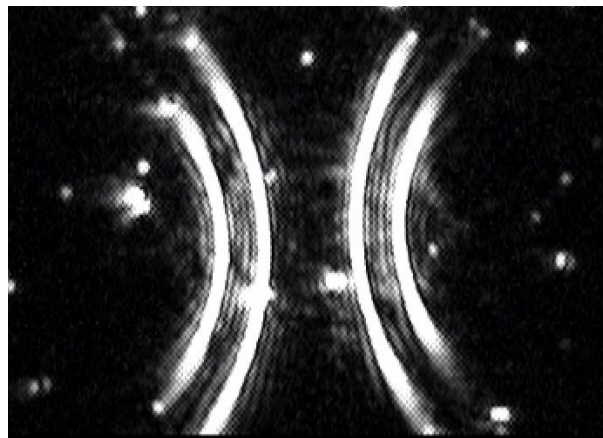
(a)



(b)



(c)



(d)

Figure 3.20: (a) a comparison between concave and convex arrangements. (b) Half parabolic gratings. (c) One set of parabolic gratings. (d) Parabolic edges only.

## Corner Resonators

It was suggested by John Pendry that a checkerboard structure with negative and positive refractive index material can form a corner resonator with a zero phase path<sup>41</sup>. The structure is shown in Fig. 3.21. Laser light is used to excite the corner scattering effect shown in Fig. 3.22. The corner scattering is different with different wavelengths. SPPs are excited at the four edges due to discontinuity. Only energy around the corner can be trapped and circled. SPPs further away from the corner will be lossy and can't be confined. The area of the corner scattering effect is decreased while the wavelength is increased from 488 nm to 532 nm. However, when the wavelength is increased to 633 nm, the scattering spot is divergent again. It shows that in the desired wavelength regime (500 nm ~ 532 nm), the resonance confinement is quite tight around the corner. This shows the possibility of making a tiny resonator with a negative refractive material.

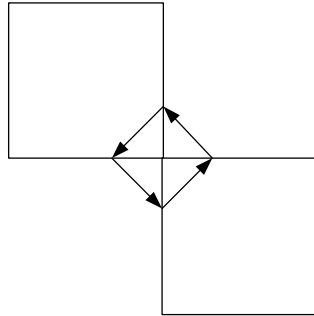
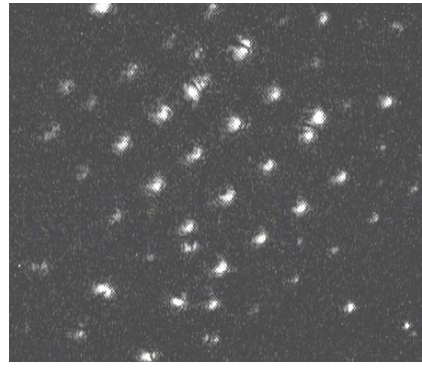


Figure 3.21: The checkerboard structure of positive and negative refractive index square.

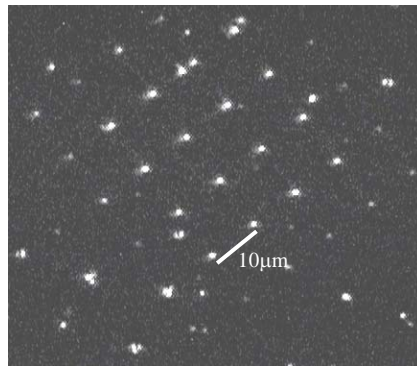




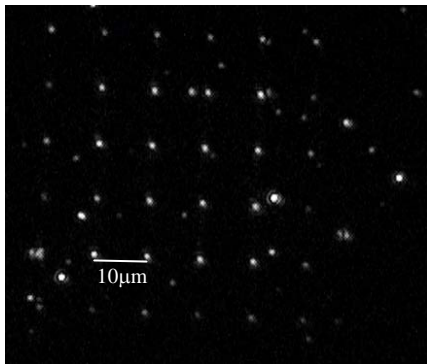
(a)



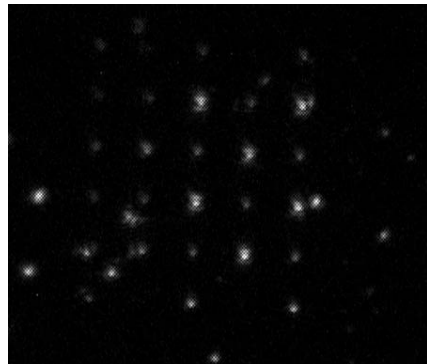
(b)



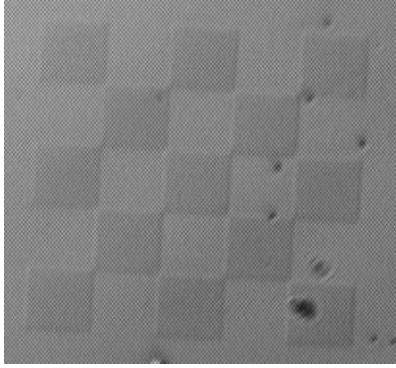
(c)



(d)



(e)



( f )

Figure 3.22: Light confinement in the corner resonator structure (a) 488 nm, 1.3 mW (b) 496 nm, 1.3 mW (c) 502 nm, 1.4 mW (d) 532 nm (e) 632 nm (f) optical image of the corner resonator, the dimension of the square is  $10\ \mu\text{m} \times 10\ \mu\text{m}$ . (d) and (e) have the same level of power and incident angle.

### *Conclusion*

In this chapter, five different structures have been demonstrated to show that negative refractive properties exist in the nano-grating region. With a simplified ray-tracing model, the paths in the designed patterns can be understood. There is currently no isotropic medium that demonstrates a negative refraction effect. Several groups have demonstrated negative refraction in highly anisotropic systems, which are challenging in fabrication. Our 2D plasmonic devices offer one possibility to demonstrate negative refractive index effects in easily fabricated structures.

# Chapter 4: Fluorescence Enhancement using Surface Gratings

## Introduction

In this chapter, fluorescence material on the surface gratings is studied. The general idea is that the strong surface field helps enhance the fluorescence efficiency. Possible applications involve bio-detection and plasmonic amplification devices. In order to achieve the most efficient fluorescence emission, we need a good understanding of how fluorescent molecules behave in various experimental geometries, especially in close proximity to metal and dielectric interfaces. In many previous papers (see for example<sup>42~49</sup>), the radiation patterns of fluorescent molecules deposited on dielectric/dielectric or dielectric/metal interfaces have been calculated and observed. However, much work remains to be done on development of the most efficient geometries for fluorescence detection. For example, a collection lens may be designed according to the angular distribution of the emitted signal<sup>47</sup>.

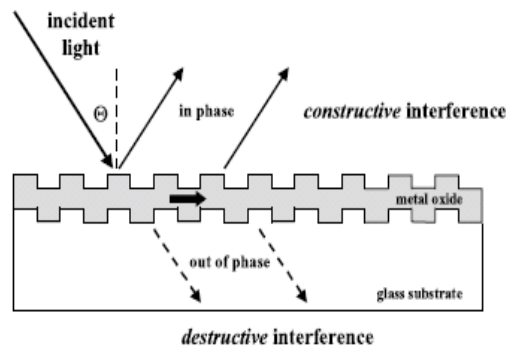


Figure 4.1: Evanescent wave coupling structure.

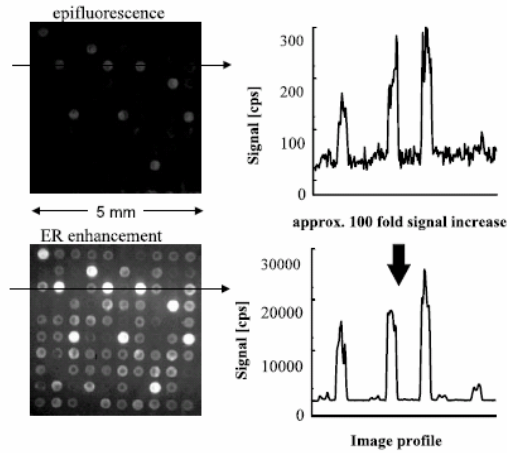


Figure 4.2: Fluorescence efficiency between precise angle coupling and arbitrary angle coupling<sup>50</sup>.

Alternatively, evanescent wave (EW) structures have been suggested as shown in Fig.4.1, which considerably enhance fluorescence through enhanced coupling to evanescent waves as shown in Fig.4.2<sup>50</sup>. Lakowicz *et al.* demonstrated<sup>51 ~ 54</sup> that the fluorescent signal can be excited more by utilizing surface-plasmon coupled emission (SPCE) shown in Fig. 4.3 (note however, it was reported<sup>55 ~ 57</sup> that the fluorescence signal can be either suppressed or enhanced by the existence of a metal film). In both the EW and the SPCE structures, sensitive optical designs must be carefully implemented. Fig. 4.4 shows that the evanescent wave needs to be coupled at a precise angle; while the collection angle for SPCE covers a cone with a large semi-vertical angle, and can be inconvenient to collect as shown in Fig. 4.5. In this chapter we propose and study another type of fluorescence detection geometry in which the fluorescence signal is enhanced by at least a factor of 10 compared to more usual geometries, yet does not require any complicated optical arrangement, so that a regular commercial fluorescence optical microscope (FOM) may be used. In our geometry the fluorescence enhancement is achieved through enhancement of pumping light at the substrate because of surface plasmon excitation facilitated by

dielectric surface gratings. The studied geometry may be potentially useful in sensing applications.

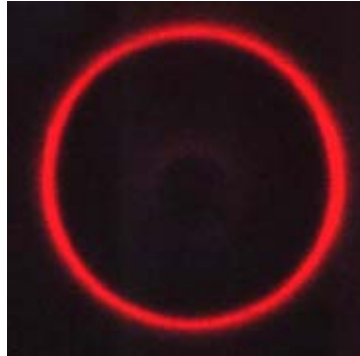


Figure 4.3: Surface-Plasmon Coupled Emission<sup>53</sup>.

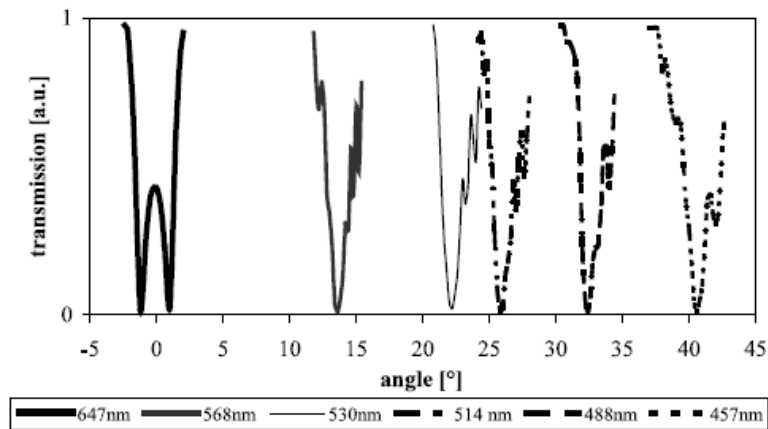


Figure 4.4: Coupling angle for each laser wavelength. When transmission is close to zero, the energy is coupled into the waveguide mode. For each wavelength, the angle is critical<sup>50</sup>.

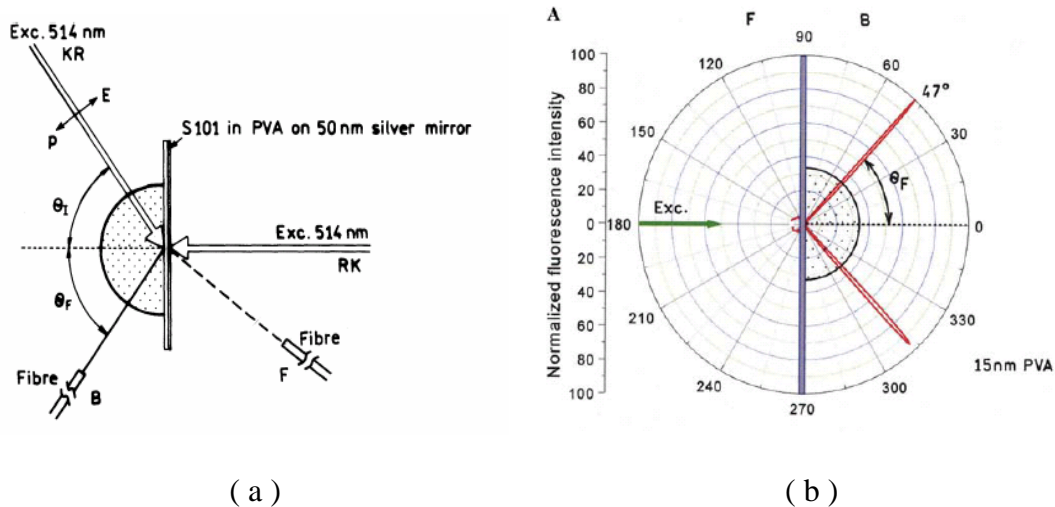


Figure 4.5: (a) Surface-Plasmon Coupled Emission setup and (b) the emission angle. The pumping light is incident normally and the emission is at  $47^{\circ}$ <sup>53</sup>.

## Experiment

### *Comparison between a Grating Deposited onto a Metal Layer and an Evanescent Grating Coupler*

Our device geometry is shown in Fig. 4.6. A layer of fluorescent material (R6G) dissolved in ethanol has been spin-coated onto a PMMA grating. 100 nm thick PMMA nano-stripe gratings have been formed by E-beam lithography on top of two kinds of substrates: an ITO/Glass and an Au/Glass substrates, as shown in Fig. 4.6(a) and (b), respectively. The thickness of the Au layer was about 50 nm. The typical periodicity of the PMMA stripe gratings shown in Fig. 4.7(a) was 500 nm. Fig. 4.7(a) and (b) shows the AFM image of the PMMA grating and how the gratings were arranged on the surface of our samples, respectively.

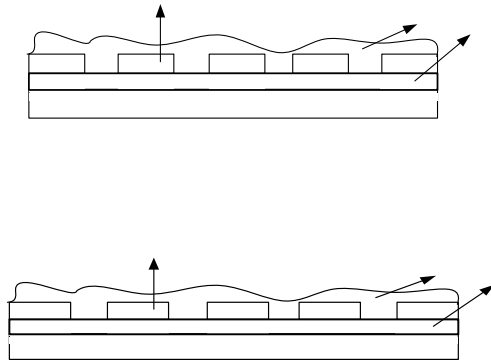
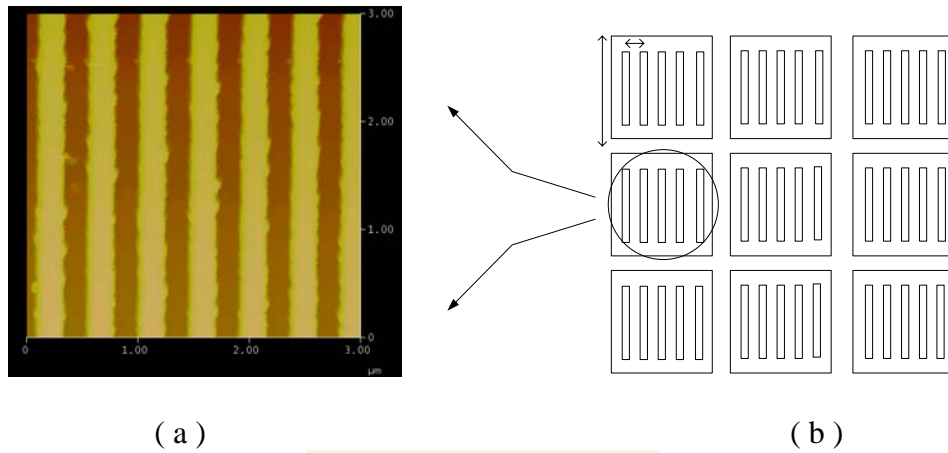
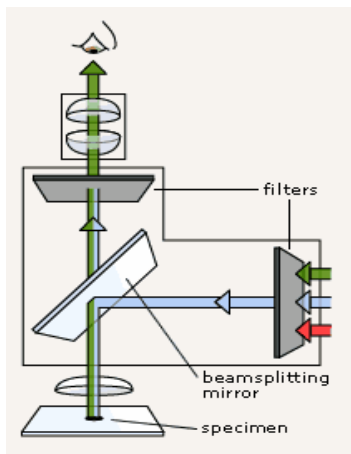


Figure 4.6: Device structures (a) ITO substrate (b) Gold substrate.



(a)

(b)



(c)

Figure 4.7: (a) AFM image of the nano-stripe gratings; (b) Dimensions of the pattern (c) Fluorescence Optical Microscope.

All samples have been examined under a Leica MZ FLIII fluorescence stereomicroscope (FSM) as shown in Fig. 4.7(c). The FSM is located on the 6<sup>th</sup> floor of Plant Science Building. The wavelength of the excitation filter is centered at 560 nm with 40 nm bandwidth. The emission barrier filter is located at 610 nm. The emission peak of R6G (in ethanol) is 590 nm. The results are shown in Fig. 4.8. Fig. 4.8 (a) corresponds to R6G on ITO substrates. Fig. 4.8 (b) was taken with R6G on an Au film substrate. The sample surfaces were prepared using the same procedure, and the images were taken with identical exposure times and gains of the CCD camera from Diagnostic Instruments. In order to analyze our data numerically, we have extracted the digital values of the signal for each pixel of the JPEG image file produced by the CCD camera, and compared the ratios of the digital values (DV) at different pixels. Note that these ratios have to be analyzed by taking into account the gain factor  $\Gamma$  of the CCD camera. Typical values of  $\Gamma$  range from 0.45 to 2.5, and the light intensity is related to the digital value (DV) according to  $Intensity = const \cdot (DV)^\Gamma$ . The CCD of the fluorescence microscope used in our experiments was set at  $\Gamma \sim 2.2$  in order to emulate the response of the human eye. Fig. 4.8 shows that the fluorescence of R6G deposited on top of the unperturbed PMMA layer (without a grating) is barely detectable. Compared to the grating on the ITO substrate, the fluorescence is enhanced by at least a factor of 10 (the ITO patterns have some defects so there are some dark dots on the grids). In this example, we have not yet optimized the grating pitch and the excitation polarization. Since fluorescence microscopes are commonly used in bio-detection, these results already indicate the competitive potential of our geometry in bio-sensing applications. From a report<sup>55</sup> the authors claimed that much emission will be quenched by a metal film, so the total emission power on a



metallic system ( water / fluorophore dipole / metal / glass ) is lower than that in an evanescent enhancement structure ( water / fluorophore dipole / glass ). However, the authors didn't consider the experimental limit. That is to collect the all-angle distributed emission need optical components which make the examination difficult. The device platform proposed here doesn't have this problem. Although no simulation is performed here, the experimental results already show the possible applications.

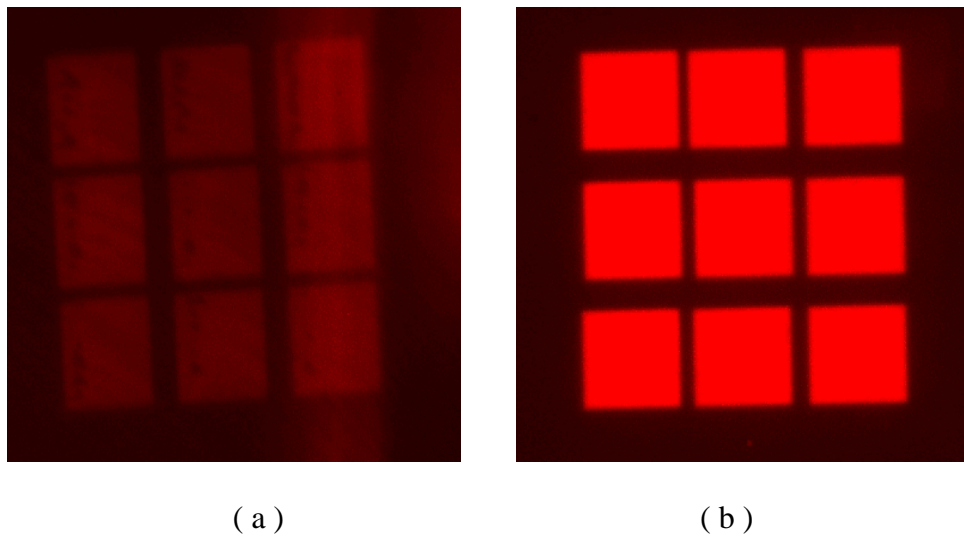


Figure 4.8: The intensity comparison of R6G/PMMA gratings on (a) ITO/glass substrate; (b) Au/glass substrate.

### *Polarization and Periodicity Dependence*

In order to understand how the fluorescence signal taken with the FSM is affected by the periodicity of the gratings, we made a sample with regions of different periodicity varying from 400 nm to 1  $\mu\text{m}$ . The experimental setup is shown in Fig. 4.9. Polarization dependence was studied first.

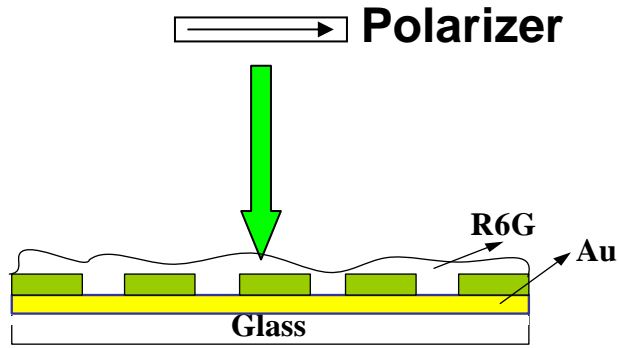
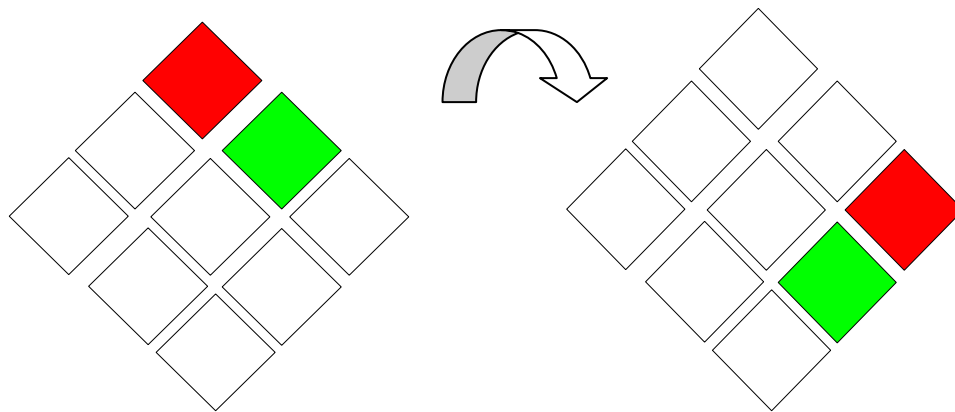


Figure 4.9: Polarization setup

The sample geometry is illustrated in Fig. 4.10 (a), in which the grating periodicity is given in nanometers. Figs. 4.10 (b, c) indicate that the fluorescence enhancement depends strongly on the grating periodicity. A mercury lamp filtered by a film polarizer was used as the excitation source at normal incidence. The sample was rotated so that the polarization direction was changed with respect to the grating trenches. The results of these experiments are shown in Figs.4.10 and 4.11.



( a )  $90^\circ$  rotation of the sample

Figure 4.10 (a): Fluorescence under normal excitation - the arrangement of grating periodicity ( in nanometers ).

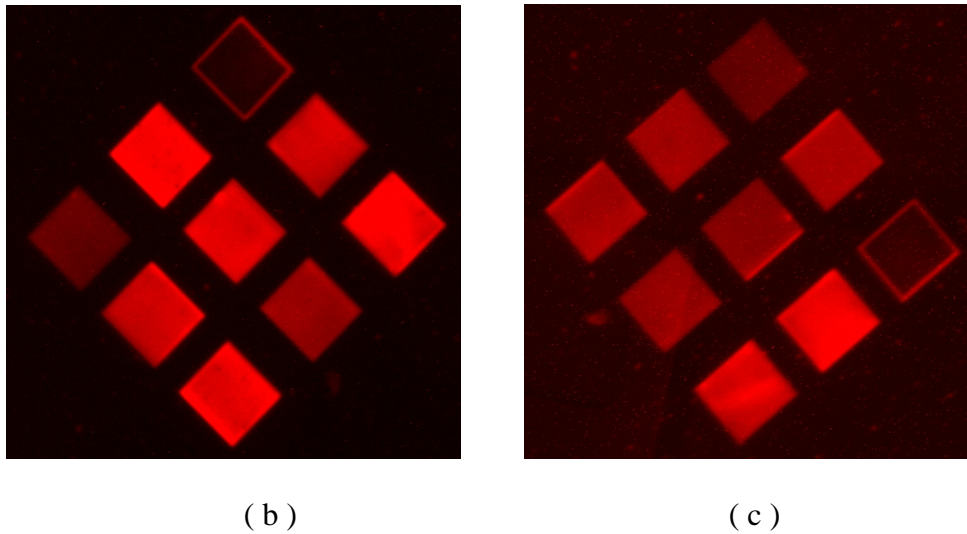


Figure 4.10: Fluorescence under normal excitation - (b) FSM pictures taken under the polarized Hg Lamp. The E field is parallel to the grating trenches (exposure time: 250 s). (c) The sample was rotated  $90^\circ$  clockwise. The E field is perpendicular to the grating trenches (exposure time: 700 s).

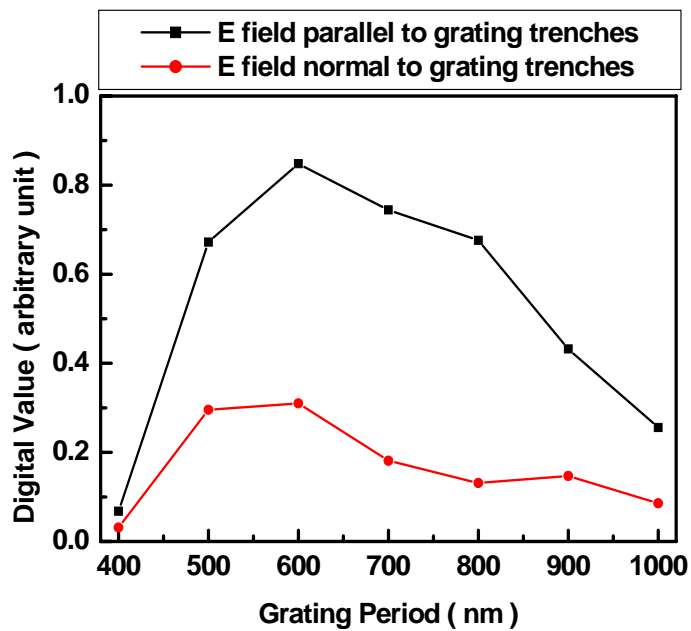


Figure 4.11: Polarization effect on gratings with normal incidence to the sample surface.

The exposure time for Fig. 4.10 (b) and (c) was 250 s and 700 s respectively. Fig. 4.11 shows the normalized digital value taken from the images. Every value is normalized to the background and the exposure time. The fluorescent efficiency is 10 times higher when the E field is parallel to the grating trenches, which can be generally explained as shown in Fig. 4.12.

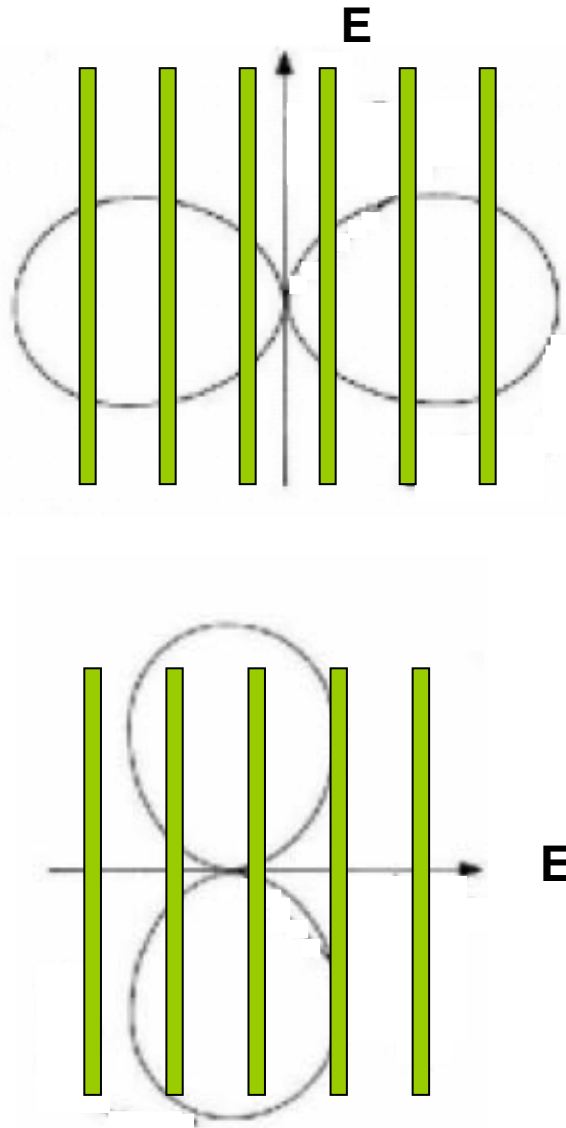


Figure 4.12: the polarization effect on the sample.

When the dipole radiation lobe is interacted with the grating stripes, the emission angle is converted to the normal direction. Therefore, a higher portion of the emission light can be detected. In order to study the enhancement mechanism in more detail we have studied how the excitation angle affects the fluorescence excited at various grating periodicities.

### *Rotation of Incident Angle*

A one-dimensional (1D) PMMA grating on an Au film surface acts like a 1D plasmonic crystal<sup>56</sup>. In order to relate the fluorescence enhancement with the plasmonic crystal properties of our substrates we have performed more detailed measurements of fluorescence at different angles of the excitation light. In these experiments the incident laser light was tilted at an angle  $\theta$  with respect to the z-axis and rotated by an angle  $\alpha$  with respect to the y-axis in the x-y plane as shown in Fig. 4.13. The emission intensity of each pattern is recorded with the  $\alpha$  rotation of every 10 degrees. Fig. 4.14 shows two patterns illuminated at different rotation angles  $\alpha$ . In Fig.4.14 (a), 411 nm and 840 nm patterns emit efficiently, while in Fig.4.14 (b), the most efficient fluorescence comes from the 693 nm pattern. Fig.4.14 (c) indicates the arrangement of the gratings. The fluorescence signal measured as a function of angle is shown in Fig.4.15 for different periodicities of the PMMA gratings. The background signal was subtracted from every data point and normalized to the CCD exposure time. The angle  $\alpha$  is scanned from -10 to 90 degrees.

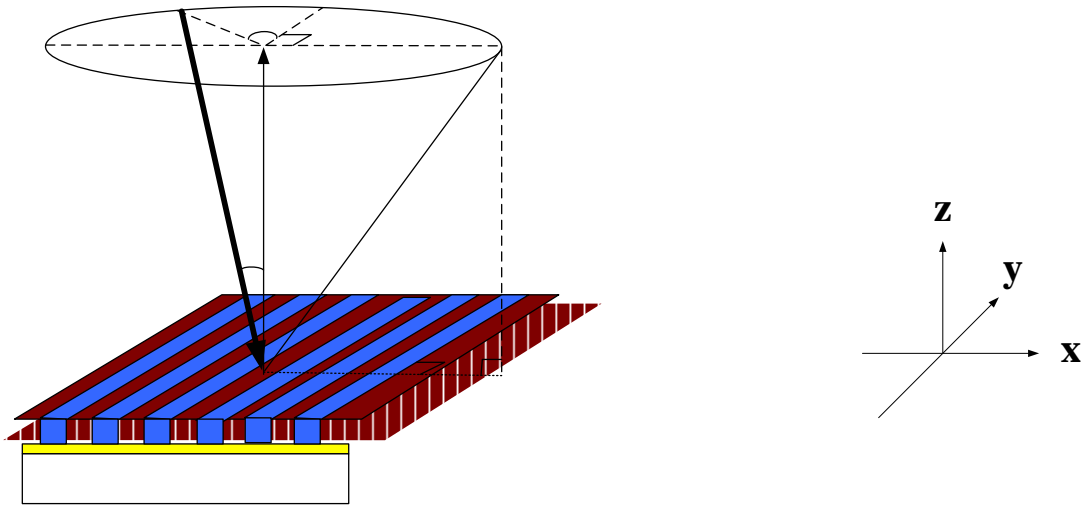


Figure 4.13: The geometry of the incident laser beam and angle definitions.

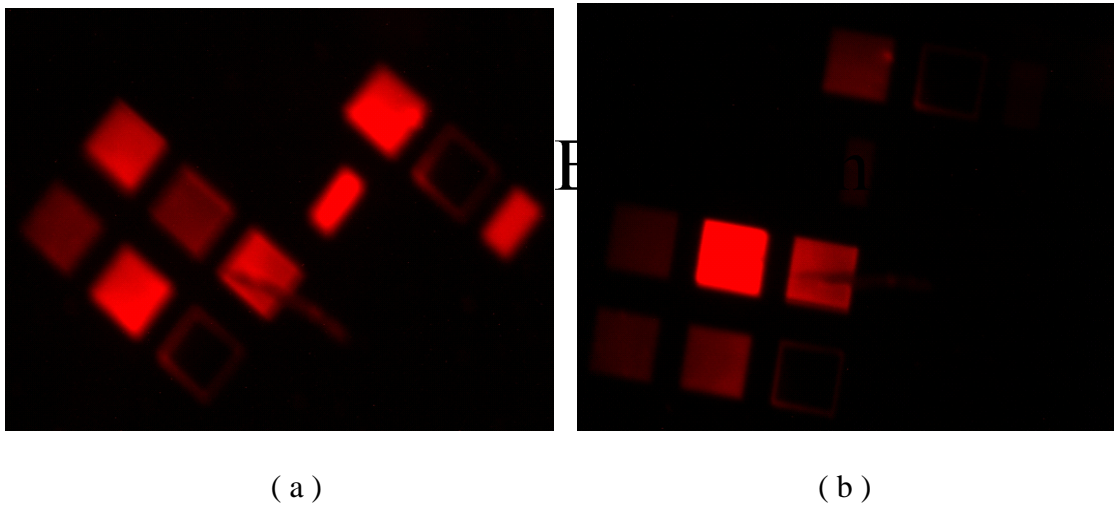
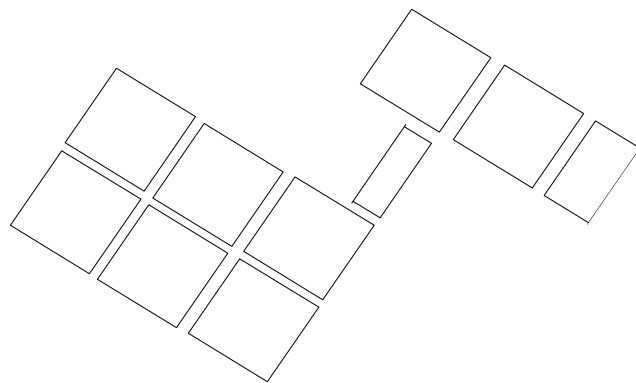


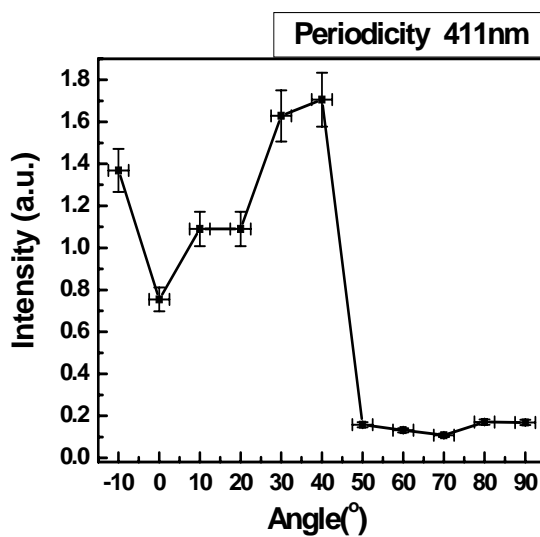
Figure 4.14: (a)  $\alpha = 30^\circ$  and patterns with 841 nm and 411 nm periodicity are excited most strongly. (b)  $\alpha \sim -2^\circ$  and the pattern with 693 nm periodicity fluoresce most strongly.

R6G



(c)

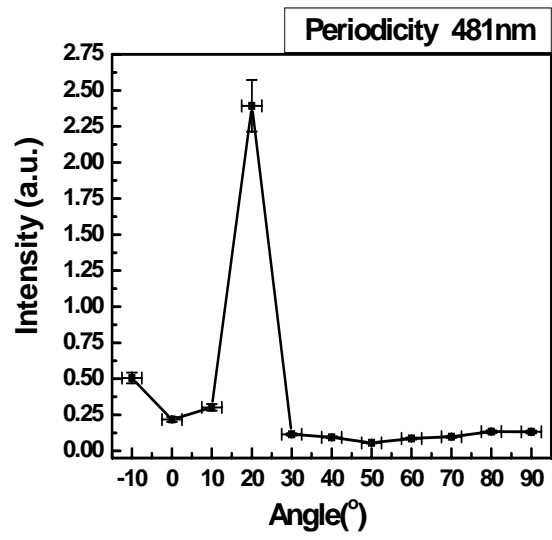
Figure 4.14: (c) The pattern arrangement of (a) and (b).



(a)

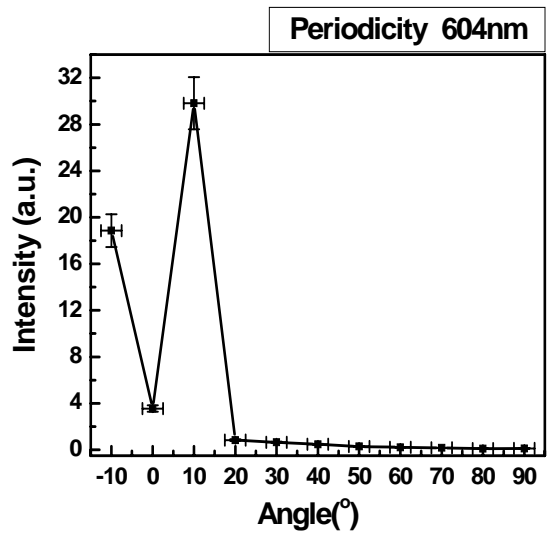
Figure 4.15: Fluorescence emission vs. angle  $\alpha$ : (a) Periodicity – 411 nm.

481



( b )

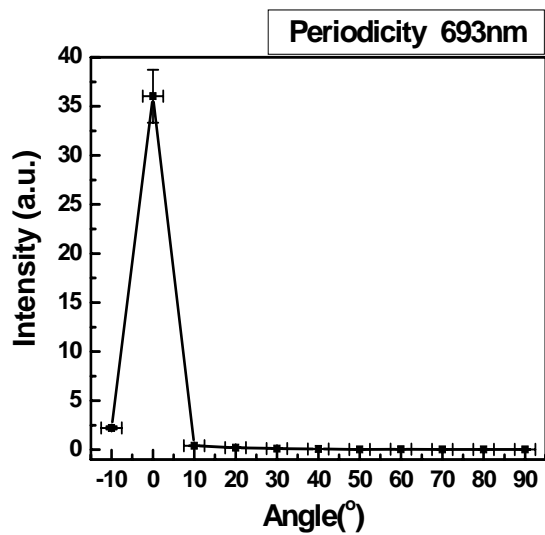
Figure 4.15: Fluorescence emission vs. angle  $\alpha$ : (b) Periodicity – 481 nm.



( c )

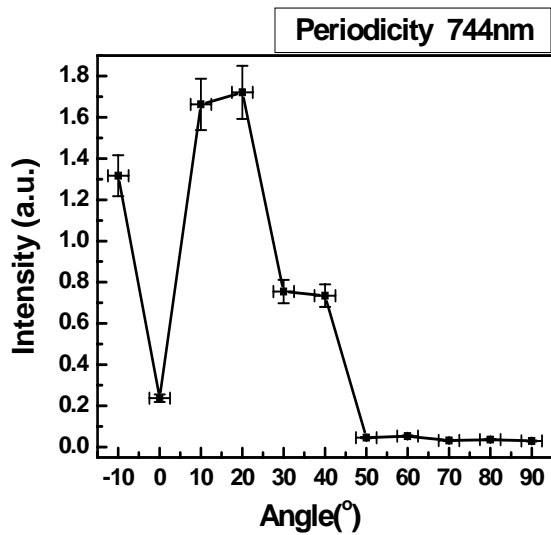
Figure 4.15: Fluorescence emission vs. angle  $\alpha$ : (c) Periodicity – 604 nm.





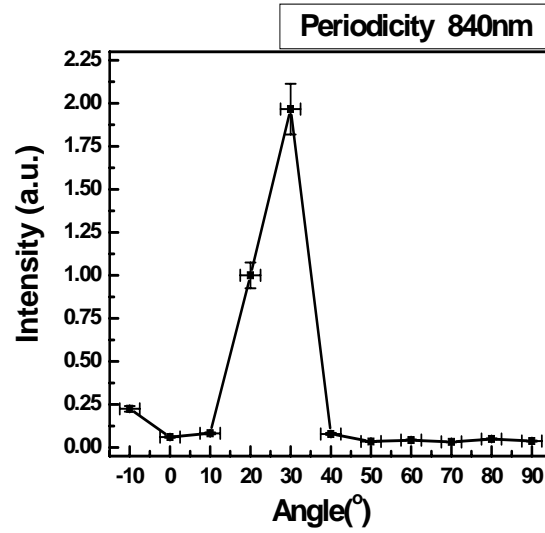
( d )

Figure 4.15: Fluorescence emission vs. angle  $\alpha$ : (d) Periodicity – 693 nm.



( e )

Figure 4.15: Fluorescence emission vs. angle  $\alpha$ : (e) Periodicity – 744 nm.



( f )

Figure 4.15: Fluorescence emission vs. angle  $\alpha$ : (f) Periodicity – 840 nm.

### Discussion

The angle  $\alpha$ , which corresponds to the maximum of the fluorescence signal, can be determined from Fig. 4.15. The error of the measured angle is in the range of  $\pm 2.5^\circ$ . The reason for the unsymmetrical intensity at  $-10^\circ$  and  $+10^\circ$  is that  $\alpha$  is not accurately tuned to a symmetrical position. To explain the angle effect, the incident wave vector

$k_o (= 2\pi/532nm)$  is decomposed as the projected wave vector  $k_o \sin \theta$  on the  $x$ - $y$  plane and

$k_o \cos \theta$  along the  $z$ -axis.  $k_o \sin \theta$  can be decomposed into  $x$  and  $y$  components as

$k_o \sin \theta \sin \alpha$  and  $k_o \sin \theta \cos \alpha$ , respectively. The grating  $k$  vector  $2\pi m/a$  is added up along the

$x$  direction shown in eq.(17), while the  $y$  component remains unchanged as shown in

eq.(18). If a SPP is excited, the  $k$  vector of incoming photons mediated by gratings

should match the  $k$  vector of surface plasmons as shown in eq.(19).

$$k_x^* = k_o \sin \theta \sin \alpha + (2\pi n/a) = k_{sp}^\perp \quad (17)$$

$$k_y^* = k_o \sin \theta \cos \alpha = k_{sp}^\parallel \quad (18)$$

$$(k^*)^2 = (k_o \sin \theta \cos \alpha)^2 + (k_o \sin \theta \sin \alpha + 2\pi n/a)^2 = (k_{sp})^2 \quad (19)$$

where  $n$  is an integer.  $k^*$  is the composite  $k$  value on  $x$ - $y$  plane. The incident angle  $\theta$  was about  $44^\circ$ . The angle  $\alpha$  is determined from the peak intensity shown in Fig. 4.15. The detailed vector analysis is shown in Fig. 4.16. The theoretical  $k_{sp}$  for long-range SPPs on the vacuum/Au interface is  $2\pi \cdot 10^6 \cdot 2.087m^{-1}$  at 532 nm. Fig. 4.17 shows  $k^*$  for  $n=-2, -1, 0$ , and 1. At least one good integer order  $n$  is fitted to the theoretical  $k_{sp}$  for every periodicity. Table 4.1 shows the maximum excitation angle  $\alpha$ , the coupling order  $n$ , and the maximum image intensity for each periodicity. The image intensity for each period is comparable to each other because it is normalized to the exposure time. For 604 nm and 693 nm, the coupling order is  $\pm 1$ , which shows a higher fluorescence intensity compared to other gratings for which only one diffraction order is coupled efficiently.

In this surface grating structure the surface corrugation is quite shallow ( $\sim 100$  nm). Wet bio-detection on this kind of device will require that this be taken into account. A possible biodetection geometry will involve the immobilization of specific proteins, RNA or DNA molecules on the surface structure. Mass production methods such as embossing, printing and photolithography are commonplace, so that the cost of the sample substrate is low. Our design is applicable in the gene chip industry.

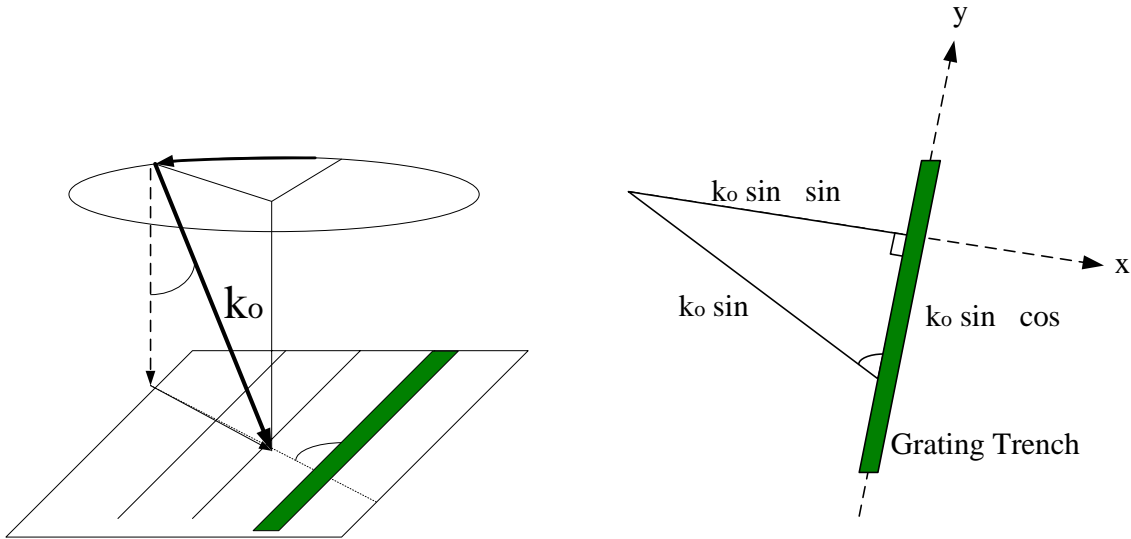


Figure 4.16: Illustration of momentum matching condition.

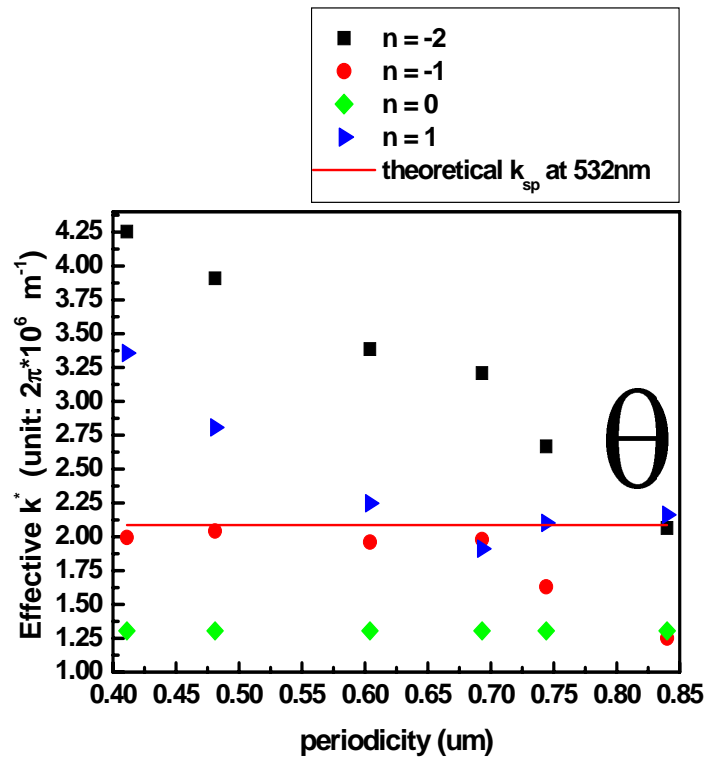


Figure 4.17:  $k^*$  for different order  $n$

Periodicity (nm)	411	481	604	693	744	840
$\alpha$ ( degrees, max fluorescence)	35	20	-2	8	15	30
Ideal $\alpha$ ( degrees )	31	18	-1.2, 1.2	-8.7, 8.7	14	29, 23
Order n	<b>-1</b>	<b>-1</b>	<b>-1, +1</b>	<b>-1, +1</b>	<b>1</b>	<b>-2, +1</b>
Max intensity (a.u.)	1.7	2.4	<b>29.8</b>	<b>36.0</b>	1.7	2.0

Table 4.1: The relation between the coupling order  $n$  and the digital value of the image intensity.

## Chapter 5: Conclusion

Basic transmission properties of PMMA nano-gratings on an Au film substrate have been measured and the conditions for SPP excitation have been described. This kind of grating coupler can be viewed as a plasmon generator. A 2-D PMMA parabolic mirror patterned on an Au film was used as an energy concentrator, which serves as a coupler to couple SPPs into a curved waveguide with 138nm in width and 4 $\mu$ m in radius. Since SPPs have short effective wavelength, with this kind of coupler, light is easily coupled into small dimensional devices. In a further demonstration, the transparent glass substrate was replaced by a nonlinear glass substrate, chalcogenide glass. A layer of gold film was deposited on the slow nonlinear substrate. With a two beam interference method, a photoinduced diffraction grating was formed at the interface between the chalcogenide glass and the gold film. After the grating was formed, a probe beam was sent in. An induced transparent effect was shown. A future experiment on this topic will be to replace the slow material with fast one. Self-induced transparency should be observed. It could possibly be used as an optical switch device.

A different regime of the dispersion relation has also been studied. Because of the imaginary part of the dielectric constant of gold, surface plasmons perceive a PMMA/Au interface as a negative refractive index system. Many interesting phenomena have been observed. It was previously claimed that with a highly anisotropic layered structure, the high spatial frequency  $k$  vectors scattered from an object can be preserved in an imaging system and the conventional diffraction limit defeated. In my thesis, this kind of layered structure, a so-called “hyperlens” or “superlens”, has been demonstrated and the results

verify theoretical predictions. A real negative refraction phenomenon was demonstrated on the designed sample. A beam of SPPs was sent into a region with an effectively negative refractive index and the refraction angle was found to be negative according to Snell's Law. The results show that the figure of merit is better than that for a double negative material ( $\epsilon$  and  $\mu$  negative). This means that the propagation length can be as large as 10  $\mu\text{m}$  in the visible frequency range, which is good enough to demonstrate the various properties of negative index devices. A proof of concept on corner resonators has also been demonstrated. It shows the possibility of making a tiny resonator with zero phase paths in the cavity.

An enhanced surface field is excited on R6G/PMMA gratings/Au substrate. The pumping light converted to SPPs greatly increases the emission 10-fold higher compared to a sample with a R6G/PMMA gratings/Glass platform, a transparent substrate. This device with a R6G/PMMA gratings/Au platform has two advantages: 1. the pumping light is coupled into SPP modes which excite the dyes strongly, 2. the emission light is converted to the normal direction such that it makes the examination easy under a fluorescence optical microscope. Further experiments can be performed, such as adding different grating pitches on the x-y plane, so that different dyes show different excitation at various orientations. Different molecules can be bound to different regions of the device, for example, one kind of molecules can be bound to the PMMA grating stripes and another kind of molecules can be attached to the exposed Au in the grating region. With different pumping wavelengths, two different emissions show up. Therefore, within the same device region, two different molecules can be characterized. These kinds of

devices have great potential for application in the gene chip industry.



## Bibliography

1. T.W. Ebbesen, H.J. Lezec, H.F. Ghaemi, T.Thio and P.A. Wolf, “*Extraordinary optical transmission through subwavelength hole arrays,*” Nature, 391, P667~669, 1998.
2. William L. Barnes, Alain Dereux and Thomas W. Ebbesen, “Surface Plasmon subwavelength optics,” Nature, 424, P824~830, 2003.
3. H.A Bethe, “Theory of diffraction by small holes,” Physical Review, 66, 163~182, 1944.
4. Yu-Ju Hung, Igor I. Smolyaninov, and Christopher C. Davis, “*Strong optical coupling effects through a continuous metal film with a surface dielectric grating*”, Proc.SPIE Vol. 5927, pp. 386-394, Aug. 2005.
5. Dieter Neuschafer, Wolfgang Budach, Christoph Wanke, Salah-Dine Chibout,” *Evanescent resonator chips: a universal platform with superior sensitivity for fluorescence-based microarrays,*” Biosensors and Bioelectronics 18, pp 489-497, 2003. 42. Joseph R Lakowicz, Joanna Malicka, Ignacy Gryczynski, Zygmunt Gryczynski and Chris D Geddes, “*Topical Review: Radiative decay engineering: the role of photonic mode density in biotechnology,*” Journal of Physics D: Applied Physics, 36,pp 240-249, 2003.
6. Joseph R. Lakowicz, “*Radiative decay engineering 3: surface plasmon-coupled directional emission,*” Analytical Biochemistry 324, pp. 153-169 (2004)
7. C.D. Geddes, Z. Gryczynski, J. Malicka, I. Gryczynski, and J.R. Lakowicz,” *Fluorescence News- Directional Surface Plasmon Coupled Emission,*” Journal of Fluorescence, Vol.14, No.1, pp. 119-123 (2004).

8. Joseph R. Lakowicz, “*Radiative decay engineering 5: metal-enhanced fluorescence and plasmon emission*,” *Analytical Biochemistry* 337, pp. 171-194 (2005).
9. Henri J. Lezec and Tineke Thio, “*Diffraction evanescent wave model for enhanced and suppressed optical transmission through subwavelength hole arrays*,” *Optics Express*, Vol. 12, No. 16, P3629~3651, 2004.
10. Igor I. Smolyaninov, Yu-Ju Hung, and Christopher C. Davis, “*Magnifying superlens in the visible frequency range*”, *Science*, Vol.315, 23 March 2007.
11. J.B. Pendry, “*Negative Refraction Makes a Perfect Lens*,” *Physical Review Letters*, Vol.85, No.18, pp.3966, 2000.
12. Zubin Jacob, Leonid V. Alekseyev and Evgenii Narimanov, “*Optical Hyperlens: far-field imaging beyond the diffraction limit*,” *Optics Express*, Vol.14, No.18, pp. 8247, 2006.
13. Quirino Balzano, Yu-Ju Hung, Igor I. Smolyaninov, and Christopher C. Davis, “*Fourier Analysis of Plasmon Polariton Propagation in Periodic structures of nanoholes*,” paper JTuC108 presented at CLEO2005.
14. Suntak Park, Gwansu Lee, Seok Ho Song, Cha Hwan Oh, and Pill Soo Kim, “*Resonant coupling of surface plasmons to radiation modes by use of dielectric gratings*,” *Optics Letters*, Vol. 28, No.20, P1870~1872, 2003.
15. Jaewoong Yoon, Gwansu Lee, Seok Ho Song, Cha Hwan Oh, and Pill Soo Kim, “*Surface-plasmon photonic band gaps in dielectric gratings on a flat metal surface*,” *Journal of Applied Physics*, Vol. 94, No. 1, P123~129, 2003.

16. Armando Giannattasio, Ian R. Hooper, and William L. Barnes, “*Transmission of light through thin silver films via surface plasmon-polaritons*,” Optics Express, Vol. 12, No. 24, P5881~5886, 2004.
17. Nicolas Bonod, Stefan Enoch, Lifeng Li, Evgeny Popov, and Michel Neviere, “*Resonant optical transmission through thin metallic films with and without holes*,” Optics Express, Vol. 11, No. 5, P482~490, 2003.
18. G. I. Stegeman, J.J. Burke and D. G. Hall, “*Surface-polariton like waves guided by thin, lossy metal films*,” Optics Letters, Vol. 8, No. 7, P383~385, 1983.
19. -1. Handbook of Chemistry and Physics, CRC Press, Boca Raton, 68th Ed. 1987.  
-2. Handbook of optical constants of solids. E.D. Palik, Academic Press 1998.
20. A.V. Kats and A.Yu. Nikitin, “*Analytical treatment of anomalous transparency of a modulated metal film due to surface plasmon-polariton excitation*,” Physical Review B 70,235412, 2004.
21. Igor I. Smolyaninov, Yu-Ju Hung, and Christopher C. Davis, “*Surface plasmon dielectric waveguides*”, Applied Physics Letters, 87, 241106, (2005).
22. Igor I. Smolyaninov, Jill Elliott, Anatoly V. Zayats, and Christopher C. Davis, “*Far-field optical microscopy with a nanometer-scale resolution based on the in-plane image magnification by surface plasmon polaritons*”, Physical Review Letters, 94, 057401 (2005).
23. Wataru Nomura, Motoichi Ohtsu, and Takashi Yatsui, “*Nanodot coupler with a surface plasmon polariton condenser for optical far/near-field conversion*”, Applied Physics Letters 86, 181108 (2005).
24. William A. Challener, Christophe Mihalcea, Chubing Peng, and Kalman Pelhos,

- “Miniature planar solid immersion mirror with focused spot less than a quarter wavelength”*, Optics Express, Vol. 13, No.18, pp. 7189-7197 (2005).
25. J.J. Burke, G.I. Stegeman, and T.Tamir *“Surface-polariton-like waves guided by thin,lossy metal films,”* Physical Review B, Vol.33, No.8, pp. 5186, 1986.
26. Igor I. Smolyaninov, Yu-Ju Hung and Christopher C. Davis, *“Light-induced resonant transmittance through a gold film,”* Applied Physics Letters, 87, 041101, 2005.
27. V.G. Veselago, *“The electrodynamics of substances with simultaneously negative values of  $\epsilon$  and  $\mu$ ,”* Soviet Physics Uspekhi, Vol.10, No.4, pp. 509, 1968.
28. P.M. Valanju, R.M. Walser, and A.P. Valanju, *“Wave refraction in negative-index media: always positive and very inhomogenous,”* Physical Review Letters, Vol. 88, No. 18, 187401, 2002.
29. J.B.Pendry and D.R. Smith, comment on *“Wave refraction in negative-index media: always positive and very inhomogeneous,”* Physical Review Letters, Vol.90, No.2, 029703, 2003.
30. D.R.Smith, D.Schurig, and J.B.Pendry, *“Negative refraction of modulated electromagnetic waves,”* Applied Physics Letters, Vol.81, No.15, pp.2713, 2002.
31. Mark I. Stockman, *“Criterion for negative refraction with low optical losses from a fundamental principle of causality,”* Physical Review Letters, 98, 177404, 2007.
32. Vladimir M. Shalaev, *“Optical negative-index metamaterials,”* Nature Photonics, Vol.1, pp. 41, 2007.
33. Vladimir M. Shalaev, et. al. *“Negative index of refraction in optical metamaterials,”* Optics Letters, Vol. 30, No.24, pp.3356, 2005.

34. Gunnar Dolling, Christian Enkrich, Martin Wegener, Costas M. Soukoulis, and Stefan Linden, "Simultaneous negative phase and group velocity of light in a metamaterial," *Science*, Vol. 312, pp. 892, 2006.
35. Zubin Jacob, Leonid V. Alekseyev and Evgenii Narimanov, "Optical Hyperlens: far-field imaging beyond the diffraction limit," *Optics Express*, Vol.14, No.18, pp. 8247, 2006.
36. Alessandro Salandrino and Nader Engheta, "Far-field subdiffraction optical microscopy using metamaterial crystals: theory and simulations," *Physical Review B*, 74, 075103, 2006.
37. Henri J. Lezec, Jennifer A. Dionne, Harry A. Atwater, "Negative Refraction at Visible Frequencies," *Science Express Report*, 1139266, 22 March 2007.
38. Xiebin Fan, et al., "All-angle broadband negative refraction of metal waveguide arrays in the visible range: theoretical analysis and numerical demonstration," *Physical Review Letters*, 97, 073901, 2006.
39. T. Pertsch, et al., "Anomalous refraction and diffraction in discrete optical systems," *Physical Review Letters*, Vol.88, No.9, 093901, 2002.
40. Zhaowei Liu, et al., "Far-field optical hyperlens magnifying sub-diffraction-limited objects," *Science* 315, 1686, 2007.
41. Sebastien Guenneau, Boris Gralak and J.B.Pendry, "Perfect corner reflector," *Optics Letters*, Vol. 30, No.10, pp. 1024, 2005.
42. W. Lukosz and R. E. Kunz, "Light emission by magnetic and electric dipoles close to a plane interface. I. Total radiated power," *Journal of Optical Society in America*, Vol. 67, No.12, pp. 1607, 1977.

43. W. Lukosz and R. E. Kunz, "*Light emission by magnetic and electric dipoles close to a plane interface. II. Radiation patterns of perpendicular oriented dipoles,*" Journal of Optical Society in America, Vol. 67, No.12, pp. 1615, 1977.
44. W. Lukosz "*Light emission by magnetic and electric dipoles close to a plane interface. III. Radiation patterns of dipoles with arbitrary orientation,*" Journal of Optical Society in America, Vol. 69, No.11, pp. 1495, 1979.
45. W.H.Weber and C. F. Eagen, "*Energy transfer from an excited dye molecule to the surface plasmons of an adjacent metal,*" Optics Letters, Vol. 4, No. 8 pp 236, 1979.
46. R.R.Chance, A.Prock, and R. Silbey, "*Molecular fluorescence and energy transfer near interfaces,*" in Advances in Chemical Physics, I. Prigogine and S.R. Rice, eds., pp.1-65, (Wiley, New York, 1978).
47. Jorg Enderlein, Thomas Ruckstuhl, and Stefan Seeger, "*Highly efficient optical detection of surface-generated fluorescence,*" Applied Optics, Vol. 38, No. 4, pp 724,1999.
48. Jorg Enderlein, "*Single-molecule fluorescence near a metal layer,*" Chemical Physics 247 pp 1, 1999.
49. Aldo Minardo, Romeo Bernini, Flavio Mottola and Luigi Zeni, "*Optimization of metal-clad waveguides for sensitive fluorescence detection,*" Optics Express, Vol. 14, No. 8, pp 3512, 2006.
50. Dieter Neuschafer, Wolfgang Budach, Christoph Wanke, Salah-Dine Chibout, "*Evanescent resonator chips: a universal platform with superior sensitivity for*

- fluorescence-based microarrays*,” *Biosensors and Bioelectronics* 18, pp 489-497, 2003.
51. Joseph R Lakowicz, Joanna Malicka, Ignacy Gryczynski, Zygmunt Gryczynski and Chris D Geddes, “*Topical Review: Radiative decay engineering: the role of photonic mode density in biotechnology*,” *Journal of Physics D: Applied Physics*, 36,pp 240-249, (2003).
52. Joseph R. Lakowicz, “*Radiative decay engineering 3: surface plasmon-coupled directional emission*,” *Analytical Biochemistry* 324, pp. 153-169 (2004)
53. Geddes, Gryczynski, Malicka, Gryczynski, and Lakowicz,” *Fluorescence News-Directional Surface Plasmon Coupled Emission*,” *Journal of Fluorescence*, Vol.14, No.1, pp. 119-123 (2004).
54. Joseph R. Lakowicz, “*Radiative decay engineering 5: metal-enhanced fluorescence and plasmon emission*,” *Analytical Biochemistry* 337, pp. 171-194 (2005).
55. Jorg Enderlein and Thomas Ruckstuhl, “*The efficiency of surface-plasmon coupled emission for sensitive fluorescence detection*,” *Optics Express*, Vol. 13, No. 22 pp 8855, (2005).
56. Takayuki Okamoto, Fekhra H’Dhili and Satoshi Kawata, “*Towards plasmonic band gap laser*,” *Applied Physics Letters*, Vol. 85, No.18, pp 3968, 2004.